Intergranular stress and plastic strain formation during laser scanning of an additively manufactured stainless steel: an experimentally-driven thermomechanical simulation study

Nikhil Mohanan, Juan Guillermo Santos Macías, Jérémy Bleyer, Thomas Helfer, Manas Upadhyay

Intergranular stress and plastic strain formation during laser scanning of an additively manufactured stainless steel: an experimentally-driven thermomechanical simulation study

Nikhil Mohanan[a], Juan Guillermo Santos Macías[a,1], Jeremy Bleyer[b], Thomas Helfer[c], Manas V. Upadhyay[a,*]

[a] *Laboratoire de Mécanique des Solides (LMS), Ecole Polytechnique, Institut Polytechnique de Paris, CNRS UMR 7649, Route de Saclay, 91128 Palaiseau Cedex, France*
[b] *Laboratoire Navier, Ecole des Ponts ParisTech, Université Gustave Eiffel, CNRS UMR 8205, 6 et 8 avenue Blaise Pascal, 77455 Marne-la-Vallée Cedex 2, France*
[c] *CEA, DEN/DEC/SESC, Cadarache, F-13108 Saint-Paul-lez-Durance, France*

Abstract

A novel experiment-driven modelling and simulation approach is proposed to study the formation of intergranular stresses and plastic strains during laser scanning of additively manufactured 316L stainless steel. Recently, laser scanning experiments had been performed using a unique coupling between a continuous-wave laser and a scanning electron microscope. These experiments form the basis for the development of a thermo-elasto-viscoplastic polycrystal model endowed with the minimum necessary physics of the problem in order to facilitate simulating sufficiently large domains to obtain reasonable stress magnitudes. The case of a single laser line scan performed in vacuum is analyzed in detail. Polar dislocation density magnitudes and distribution predicted from the simulation are compared with those measured experimentally. Results reveal that for 93% of the grains in the lasered zone, a statistical measure of the predicted polar dislocation density (Nye's) tensor lies within a factor of 2 (higher or lower) of the experimental one; this result sets a benchmark for future experiment-simulation comparisons. Subsequent investigation studies the origin of the local resid-

*Corresponding author
Email address: manas.upadhyay@polytechnique.edu (Manas V. Upadhyay)
[1]Current address: IMDEA Materials Institute, Eric Kandel 2, Tecnogetafe - Getafe 28906, Spain

ual stresses and plastic strains. On the lasered surface, the grain surface-averaged normal residual stress component and plastic strain component along the scan direction reaches a value ~ 1.7 GPa and 0.04, respectively. The contribution of elastic anisotropy, plastic heterogeneity and strengthening due to microstructure refinement after laser scanning on the formation of stresses and plastic strains is studied in detail.

Keywords: Crystal plasticity, 3D printing, dislocations, finite elements, modelling

1. Introduction

Metal additive manufacturing (AM) involves heat-matter interactions that result in strong thermal gradients and high heating/cooling rates. These give rise to large thermomechanical driving forces resulting in significant microstructure evolution and formation of heterogeneous intergranular residual stresses and plastic strains. The as-built microstructure and the residual stresses together determine the subsequent mechanical response and structural integrity [1]. Local (intergranular) residual stress concentrations generated during fabrication can result in local damage and crack nucleation eventually resulting in failure either during AM or under service conditions [2, 3]. It is therefore crucial to understand the generation and evolution of intergranular stress and plastic strains. Furthermore, this understanding can open new pathways to optimize process parameters to generate a desired state of residual stresses for as-built parts.

Probing their evolution locally is very challenging, especially during AM. A comprehensive understanding of these evolutions necessitates a combination of state-of-the-art microstructure characterization techniques e.g., scanning electron microscopy (SEM), synchrotron X-ray diffraction, etc., together with polycrystalline thermomechanical simulations. However, a one-to-one comparison between experiments and simulations i.e., obtaining initial and boundary conditions as well as microstructural input from experiments and comparing predictions against measurements, is critically lacking.

One of the main reasons for this lack is the difficulty involved in extracting the initial and final states of the microstructure necessary to perform a one-to-one comparison. For polycrystalline models, microstructure input and final state for comparison are predominantly obtained from scanning electron microscopy (SEM) measurements. However, it is impractical to

perform AM inside electron microscopes simply due to the inevitable contamination from feedstock addition that would critically damage the microscopes. It is also very difficult to reliably extract microstructure information using SEM from the same locations before and after an *ex situ* fabrication due to surface modification caused during AM.

A way around this problem is to perform laser scanning inside SEM microscopes without the addition of material. For this purpose, Santos Macìas et al. [4] recently developed a unique coupling between a continuous-wave (CW) laser and an SEM microscope (Figure 1a), henceforth denominated as CW Laser-SEM [4]. This device allows performing laser scanning in a controlled environment (e.g., secondary vacuum or stationary inert gas to prevent oxidation) as well as microstructure characterization before and after laser scanning without the need to re-polish samples in between measurements. Therefore, in comparison to an AM process, laser scanning inside the CW Laser-SEM offers more control over initial and boundary conditions of the problem and provides microstructural input as well as post-laser scan data for a one-to-one comparison with polycrystalline simulations.

In a recent study using this device, Santos Macías et al. [4] performed single-pass and multi-pass laser scans inside the SEM under secondary vacuum on additively manufactured 316L stainless steel. They compared electron backscatter diffraction (EBSD) images taken before and after laser scanning to precisely track the microstructural changes brought about by laser scanning. For all the laser scans that caused local melting, the subsequent analysis revealed a significant refinement of the Cr-Mo cellular segregation structures, and thus a higher yield strength, with respect to the surrounding as-built material. The experiment also revealed the formation of geometrically necessary dislocations indicating the occurrence of plastic deformation during rapid cooling. However, in that study [4], it was not possible to gain insight into the formation and evolution of intergranular stresses and strains and the contributions of microstructure refinement, elastic anisotropy and plastic heterogeneity on residual stresses and plastic strains, which requires performing simulations.

On the polycrystalline thermomechanical simulation front, significant progress has already been made in the context of studying microstructure evolution during metal AM. Lindroos et al. [5] proposed a small deformation based mechanical model to simulate the formation of residual stresses due to elastic, thermal and plastic deformation including solid-state phase transformations occurring during laser powder bed fusion of an H13 tool steel; the temperature evolution was approximated using the Rosenthal solution [6]. Meanwhile, Grilli et al. [7] proposed a finite deformation based ther-

momechanical polycrystal model coupled with a thermal fluid flow model and a phase-field based grain growth (solidification) model. This model was used by Hu et al. [8] to simulate the residual stresses and plastic deformation generated due to the cooling down of the melt during laser powder bed fusion of 316L stainless steel. More recently, Hu et al. [9] extended the mechanical part of the aforementioned model [7, 8] to incorporate dislocation density based hardening laws to study dislocation structure formation during laser powder bed fusion. Meanwhile, Kuna et al. [10] have developed a coupled cellular automata based solidification model coupled with finite deformation-based weakly coupled thermomechanical model for polycrystals to also study residual stress formation during laser powder bed fusion of 316L. Among all the aforementioned studies, only Kuna et al. [10] have compared their simulation predictions with statistical data from electron backscatter diffraction (EBSD) imaging; however, the simulated and experimental microstructures were compared from a statistical standpoint and a one-to-one comparison was impossible.

In light of the above, the aim of this work is to put together a polycrystalline thermomechanical model that has all the ingredients necessary (i) to operate at the polycrystal level, (ii) to take microstructural input from the CW laser-SEM experiments and reproduce the thermomechanical boundary conditions, and (iii) to perform laser scanning simulations and compare its predictions directly with the EBSD measurements after laser scanning. To that end, a thermo-elasto-viscoplastic (TEVP) model is constructed in a small deformation setting using an isotropic hardening law and numerically implemented in a finite element (FE) framework. This model is designed to capture the physics necessary to predict the TEVP response everywhere outside the melt pool i.e., after solidification but without modelling melt pool dynamics and grain growth. The emphasis is on simulating a domain that is sufficiently large such that any further increase in domain size would not affect the stress state in the vicinity of the laser scan track and capturing the strengthening effect due to Cr-Mo cellular structure refinement. In order to prevent an impractical computational cost and to test the domain of applicability of the simple model, complex kinetic laws such as dislocation density based hardening or coupling with thermo-fluid dynamics or solidification models are not performed. Instead, the final microstructure i.e., after laser scanning, is used as microstructural input for simulations in order to simulate the correct grain shapes. This TEVP-FE model is applied to simulate one of the laser scans performed in [4] and the predicted polar dislocation density is compared with measurements.

The structure of this article is as follows: Section 2 briefly recalls the

CW Laser-SEM setup, material, laser scanning parameters and some results presented in [4] that are useful for this work. Section 3 introduces the TEVP theory along with its FE implementation. Section 4 is dedicated to setting up the simulation using microstructure input from experiments and reproducing the experimental initial and boundary conditions. Special attention is paid to the laser scanning parameters, microstructure (grain morphology and crystallographic orientations), temperature-dependent material parameters, initial and boundary conditions, and the role of melting in determining plastic strain history, stresses and thermal strains. In section 5, first the simulation predictions are compared against experimentally measured polar dislocation density (Nye's) tensor, which is a measure for geometrically necessary dislocations. Following the comparison, the time evolution of the stresses and the plastic strains as well as their distributions in the residual state are examined. In addition, the role of the strengthening effect due to microstructure refinement in the lasered zone on the residual stresses and plastic strains is studied along with the contributions of elastic anisotropy and plastic heterogeneity of the polycrystalline 316L. Section 6 discusses the results in the context of existing literature and provides a roadmap for enhancing the model and improving the synergy with experiments. The conclusions of this study are presented in section 7.

2. Materials and experimental procedure

2.1. Material, sample and microstructure characterization before laser scanning

The material and samples are the same as those used in [4] and they are briefly recalled here.

The base material is an additively manufactured 316L stainless steel that had been built using the laser-based direct energy deposition (L-DED) process using a powder feedstock. The 316L powder had been produced from a wrought alloy with the following composition (wt%): Fe-17.34Cr-12.55Ni-2.34Mo-1.40Mn-0.49Si-0.01P with C $<$ 0.10, S $<$ 0.1 and O $<$ 0.05, via the inert gas atomization process by Oerlikon AG in Germany; during the atomization process up to 0.05wt% O could be added into the powder. Granulometry had revealed the powder size range to be between 45 µm and 90 µm. A thin-wall shaped sample of size 100 mm $\times$ 12 mm $\times$ 0.7 mm had been built via the L-DED process using a single-pass-per-layer bidirectional printing strategy with the help of a BeAM Mobile machine. The L-DED process parameters were: 250 W power, 2000 mm/s scan speed, and 6.8

g/min powder flow rate. The manufactured samples had an average layer thickness of ~ 0.2 mm.

A test specimen of dimensions $15 \times 12 \times 0.7$ mm^3 had been cut from the center of the wall. Its surface had been polished first with silicon carbide paper (320, 600, 1200, 2400, and 4000 grit) followed by polishing with 3 µm and 1 µm diamond paste and alumina suspension rated OP-A (Struers S.A.S., France) until mirror finish. EBSD measurement had been performed at the same location on the polished and electrochemically etched (using 10%vol. oxalic acid aqueous solution) sample with a step size of 1 µm prior to laser scanning, which is shown in Figure 1b.

2.2. CW Laser-SEM coupling

The post-build laser scanning experiments on the as-built 316L test specimen are performed using the recently designed CW Laser-SEM system [4, 11] (Figure 1a). The CW laser used is a SPI QUBE 200 W air-cooled fiber laser (Industrial Laser Systems, France) with 1070 nm wavelength. It has been coupled with a FEI Quanta 600 environmental scanning electron microscope (SEM). The CW laser has the following characteristics: Power 24 - 209 W, scan speed 0.01 - 20000 mm/s, spot size 45 - 500 µm, and 2-dimensional (2D) scan strategies. The spot size is regulated using the Scanlab varioscande20i type 133 (optical z). 2D scanning is possible on a relatively large area (100×100 mm^2) using the equipped Scanlab intelliscan III 20 scanner. The full range of characterization with an SEM is accessible including secondary electron, backscatter electron, and EBSD imaging capabilities. Laser power and laser spot sizes as a function of optical z were calibrated using the Gentec UP55N-40S-H9-D0 calorimeter and the femto easy BP 13.9 beam profiler. Further details on the CW Laser-SEM can be found in [4].

2.3. Post-process laser scanning and microstructure characterization

After the initial EBSD scan (Figure 1b), the sample had been subjected to five single-pass laser scans in vacuum along the building direction of the thin walls [4]. For each of these scans, the laser spot size (60 µm) and power (24 W) had been kept constant and the velocity was varied: 50 mm/s, 100 mm/s, 250 mm/s, 500 mm/s and 1000 mm/s. The scans had been spaced at a distance of $\sim$1 mm from each other so that they do not influence each other, and a dwell time of 30 s had been inserted between each scan to allow the sample to cool down to room temperature prior to the next scan.

The line scan of main interest to this work is the one that had been performed at 500 mm/s. EBSD imaging had also been performed after laser

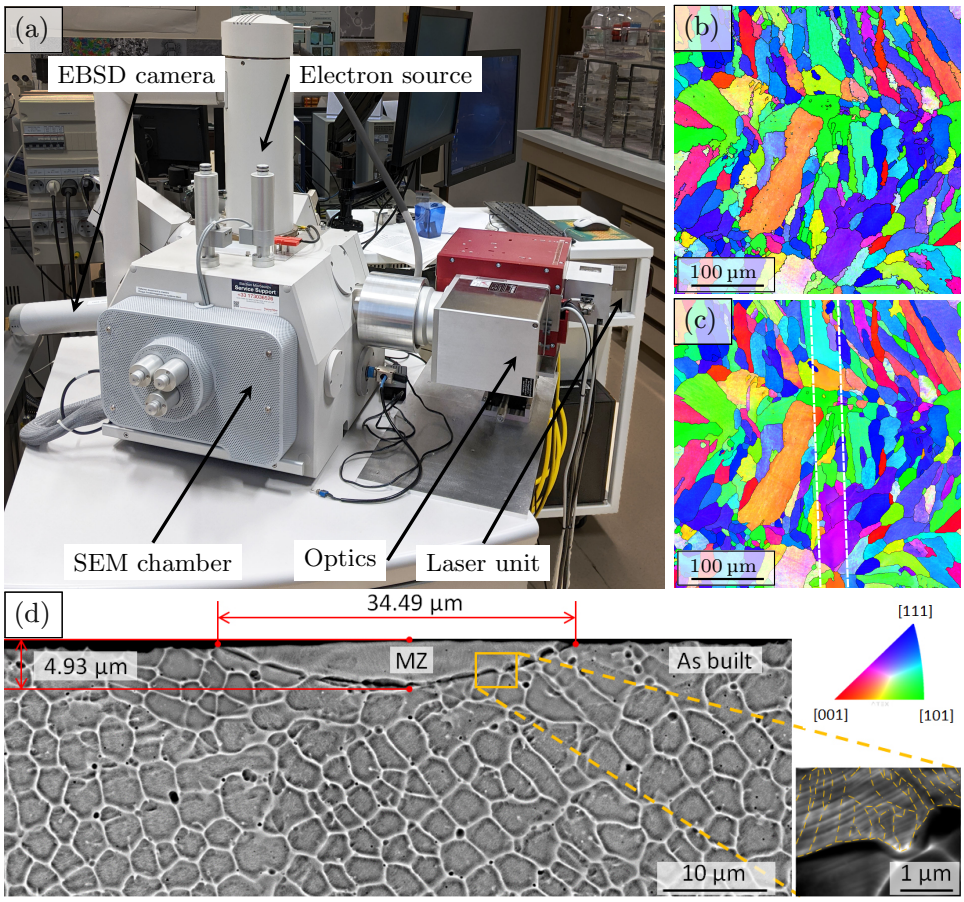

Figure 1: SEM characterization before and after laser scanning inside an SEM of an additively manufactured 316L. EBSD images using IPF z coloring taken (a) before and (b) after laser scanning at 500 mm/s. The dotted white lines in (b) demarcate the melted zone (MZ). (c) Backscatter electron (BSE) image along the cross-section after laser scanning shows the cellular microstructure refinement (Cr-Mo microsegregation cells appear in white) due to laser scanning and the measured melt pool dimensions. Images have been adapted from [4]. Note that ATEX [12] was used to interpolate data to non-indexed pixels of the EBSD images.

scanning with step sizes of 0.5 µm and 3 µm. Figure 1c adapted from [4] shows the EBSD image at a step size of 0.5 µm taken after laser scanning from the same region as the one in Figure 1b. Due to an improved surface finish after lasering, the sample did not require any preparation for the second EBSD scan. As noted in [4], this laser scanning caused conduction

mode melting along the scan track and solidification at a very high cooling rate resulting in an intragranular solute segregation cell structure in the melted zone (MZ) that is an order of magnitude smaller than the one in the as-built zone (see Figure 1d); the as-built 316L exhibits Cr-Mo solute segregation cells of size $\sim$2.2 µm and the MZ exhibits solute segregation cells of size $\sim$0.3 µm. The laser tracks did not show any signs of hot tearing. Other slower line scans result in similar features and cellular structure sizes but they are not studied in this work due to the impractical computational cost. Meanwhile, the 1000 mm/s line scan is not studied because it does not result in any melting [4], which is of main interest in this work.

This solute segregation structure refinement causes the MZ to exhibit a significantly higher strength than the as-built material [4] and the role of this strength increase is accounted during the fitting of the hardening parameters in section 4.2.

2.4. Partial Nye's tensor

An approximate polar dislocation density tensor ($\boldsymbol{\alpha}_{\text{exp}}$) was calculated from the EBSD map after lasering using the approach introduced in [13]:

$$\boldsymbol{\alpha}_{\text{exp}} = -\nabla \times \boldsymbol{g} \tag{1}$$

where $\boldsymbol{g}$ is the orientation matrix calculated from the Euler angles. This computation was performed with the help of the ATEX software [12]. Note that only 5 components of Nye's tensor are accessible from 2D EBSD data (α_{12}, α_{13}, α_{21}, α_{23}, α_{33}), and hence $\boldsymbol{\alpha}_{\text{exp}}$ is a partial Nye's tensor. These components were not computed in [4] and they are presented for the first time in section 5.1.

3. Thermo-elasto-viscoplastic finite element (TEVP-FE) model

The aim of this section is to put together the simplest TEVP model at the polycrystal level that is capable of capturing the thermomechanics (after solidification) of laser scanning described in section 2; melt pool dynamics and solidification have not been modelled. All material properties entering the equations in this section are temperature dependent and their expressions are given in section 4.1.

3.1. Kinematics

A simply connected body Ω is assumed to exist in a subset of Euclidean point space equipped with a Cartesian reference frame. The total displacement vector $\boldsymbol{u}$ and temperature θ are the four degrees of freedom considered

in this body. A small deformation framework is assumed and the total distortion $\boldsymbol{U}$, defined as $\boldsymbol{U} = \nabla \boldsymbol{u}$, is additively decomposed into elastic distortion $\boldsymbol{U}^e$, plastic distortion $\boldsymbol{U}^p$, and thermal strain $\boldsymbol{\varepsilon}^\theta$ as:

$$\boldsymbol{U} = \boldsymbol{U}^e + \boldsymbol{U}^p + \boldsymbol{\varepsilon}^\theta \tag{2}$$

The thermal strain $\boldsymbol{\varepsilon}^\theta$ is defined as:

$$\boldsymbol{\varepsilon}^\theta = \boldsymbol{\gamma}^{\boldsymbol{\theta}} \Delta\theta \tag{3}$$

where $\boldsymbol{\gamma}^\theta$ is the second order tensor of coefficient of thermal expansion (for 316L stainless steel $\boldsymbol{\gamma}^\theta = \gamma^\theta \mathbb{I}$ where γ^θ is the coefficient of thermal expansion and $\mathbb{I}$ is the second order identity tensor). $\Delta\theta = (\theta - \theta_0)$ with θ_0 being the reference temperature.

In a recent work, Lindroos et al. [14] discussed the role of solidification strains during AM of 316L.

The elastic and plastic distortions are decomposed into symmetric (elastic and plastic strains $\boldsymbol{\varepsilon}^i$) and skew-symmetric (elastic and plastic rotations $\boldsymbol{\omega}^i$) parts as follows:

$$\begin{aligned} \boldsymbol{\varepsilon}^i &= \frac{1}{2}(\boldsymbol{U}^i + \boldsymbol{U}^{iT}) \\ \boldsymbol{\omega}^i &= \frac{1}{2}(\boldsymbol{U}^i - \boldsymbol{U}^{iT}) \end{aligned} \tag{4}$$

with $i = e, p$.

The polar dislocation density (Nye's) tensor is defined as [15] :

$$\boldsymbol{\alpha} := \nabla \times \boldsymbol{U}^e = -\nabla \times \left(\boldsymbol{U}^p + \boldsymbol{\varepsilon}^\theta\right) \tag{5}$$

where $(\nabla\times)$ is the curl operator.

However, $\boldsymbol{\alpha}$ from equation (5) is not directly comparable to $\boldsymbol{\alpha}_{\mathbf{exp}}$ from equation (1) because the contribution of $\boldsymbol{\varepsilon}^e$ is not considered in the latter. To facilitate a comparison with $\boldsymbol{\alpha}_{\mathbf{exp}}$, the following entity is computed from the simulations:

$$\boldsymbol{\alpha}_{\omega^e} := \nabla \times \boldsymbol{\omega}^e \tag{6}$$

3.2. Governing equations

The first governing equation of the TEVP model is the temperature evolution equation obtained from the conservation of energy while neglecting non-mechanical heat source terms and using the energetic constitutive laws (for derivation refer to e.g., [16]):

$$\rho c_v \dot{\theta} = -\nabla \cdot \boldsymbol{q} - \theta \boldsymbol{\beta} : (\dot{\boldsymbol{\varepsilon}} - \dot{\boldsymbol{\varepsilon}}^p) + \boldsymbol{\sigma} : \dot{\boldsymbol{\varepsilon}}^p \tag{7}$$

where $(\nabla\cdot)$ is the divergence operator, c_v is the specific heat of the material at constant volume, ρ is the material density, $\boldsymbol{q}$ is the heat flux, $\boldsymbol{\beta} = \mathbb{C} : \boldsymbol{\gamma}^{\theta}$ is the thermal moduli tensor and $\boldsymbol{\sigma}$ is the Cauchy stress tensor.

The second governing equation of the TEVP model is the static equilibrium equation obtained from linear momentum conservation while neglecting body forces and inertia:

$$\nabla \cdot \boldsymbol{\sigma} = 0 \tag{8}$$

3.3. Constitutive laws

Following [16], the Neumann-Duhamel's constitutive relationship in thermoelasticity is used between the Cauchy stress $\boldsymbol{\sigma}$ and $\boldsymbol{\varepsilon}^e$:

$$\boldsymbol{\sigma} = \mathbb{C} : (\boldsymbol{\varepsilon} - \boldsymbol{\varepsilon}^p) - \boldsymbol{\beta}\ \Delta\theta = \mathbb{C} : \boldsymbol{\varepsilon}^e \tag{9}$$

For the heat flux $\boldsymbol{q}$, the well-known generalized Fourier law of heat conduction is chosen:

$$\boldsymbol{q} := -\boldsymbol{K} \cdot \nabla\theta \tag{10}$$

where $\boldsymbol{K}$ is the second-order thermal conductivity tensor dependent on temperature.

For the viscoplastic strain rate, the following well known relationship is chosen:

$$\dot{\boldsymbol{\varepsilon}}^p = \mathrm{sym}(\dot{\boldsymbol{U}}^p) = \sum_{s}^{N_{ss}} \dot{\gamma}^s\ \mathrm{sym}(\boldsymbol{m}^s) \tag{11}$$

where the sum is over all the slip systems N_{ss} for the given material phase, $\dot{\gamma}^s$ is the plastic slip rate on each slip system s, which is a non-linear function of $\boldsymbol{\sigma}$, and $\boldsymbol{m}^s := \boldsymbol{b}^s \otimes \boldsymbol{n}^s$ is the Schmid tensor for a slip system, with $\boldsymbol{b}^s$ and $\boldsymbol{n}^s$ being the Burgers vector and the slip plane normal, respectively.

Both dislocation glide and climb can be active at high temperatures. However, due to the rapid nature of the laser scanning, we posit that there is insufficient time for dislocation climb to occur due to its diffusive nature; this is also postulated in other works (see [9] and references therein). Therefore, as a first approximation, we neglect its contribution and only take dislocation glide into account. Then, $\dot{\gamma}^s$ is expressed using a power law relationship [17, 18] as:

$$\dot{\gamma}^s = \dot{\gamma}_0^s \left(\frac{|\tau^s|}{\tau_c^s} \right)^n sign(\tau^s) \tag{12}$$

where $\dot{\gamma}_0^s$ is the reference shear rate, τ_c^s is the critical resolved shear stress (CRSS), and n is the power law exponent for the slip system s.

The evolution of τ_c^s is governed by a Voce-type phenomenological isotropic hardening law [19, 20]:

$$\tau_c^s = \tau_0^s + (\tau_1^s + \Theta_1^s \Gamma)\left(1 - exp\left(-\left|\frac{\Theta_0^s}{\tau_1^s}\right|\Gamma\right)\right) \tag{13}$$

where, $\Gamma = \sum_{\delta=0}^{t}\sum_{s}^{N_{ss}} |\Delta\gamma^{s,t}|$ is the accumulated shear at a material point over time t, τ_0^s is the initial CRSS, Θ_0^s is the initial hardening rate, Θ_1^s is the asymptotic hardening rate, and $(\tau_0^s + \tau_1^s)$ is the back extrapolated CRSS.

The increment in the τ_c^s of slip system s is dependent on the shear increment of other slip systems r i.e., $\Delta\gamma^r$ and it is calculated as:

$$\Delta\tau_c^s = \frac{d\tau_c^s}{d\Gamma}\sum_{r}^{N_{ss}} h^{sr}|\Delta\gamma^r| \tag{14}$$

where h^{sr} is the hardening matrix.

The change in crystallographic orientation at a material point is taken into account by considering the increment of lattice rotations [21] as:

$$\boldsymbol{g} = \boldsymbol{g}^t \cdot \boldsymbol{R}(\Delta\boldsymbol{\omega} - \Delta\boldsymbol{\omega}^p) \tag{15}$$

where $\boldsymbol{g}^t$ is the orientation matrix from the previous time step and $\boldsymbol{R}$ is the orientation update function using the Euler-Rodrigues rotation equation [22].

3.4. Initial and boundary conditions

The initial conditions of the problem are:

$$\begin{array}{llll} \boldsymbol{u} & = \boldsymbol{u}(\boldsymbol{x}, 0) & = \boldsymbol{u}_0 & \forall \boldsymbol{x} \in \Omega \\ \theta & = \theta(\boldsymbol{x}, 0) & = \theta_0 & \forall \boldsymbol{x} \in \Omega \end{array} \tag{16}$$

where $\boldsymbol{u}_0$ is the initial displacement field and θ_0 is the initial temperature field in Ω.

The boundary $\partial\Omega$ of the domain can be divided into Dirichlet, Neumann, and Robin conditions applied respectively on $\partial\Omega_D$, $\partial\Omega_N$, and $\partial\Omega_R$. The thermomechanical boundary conditions are specified on $\partial\Omega_\theta$ and $\partial\Omega_u$ as:

$$\begin{array}{lll} \text{For energy conservation equation (7):} & & \\ \quad \theta(\boldsymbol{x}, t) & = \theta_D & \text{on } \partial\Omega_{\theta,D} \\ \quad \boldsymbol{q} \cdot \hat{\boldsymbol{n}} & = Q_N & \text{on } \partial\Omega_{\theta,N} \\ \quad \boldsymbol{q} \cdot \hat{\boldsymbol{n}} & = h(\theta - \theta_0) & \text{on } \partial\Omega_{\theta,R} \\ \text{For momentum balance equation (8):} & & \\ \quad \boldsymbol{u}(\boldsymbol{x}, t) & = \boldsymbol{u}_D & \text{on } \partial\Omega_{u,D} \\ \quad \boldsymbol{\sigma} \cdot \hat{\boldsymbol{n}} & = \boldsymbol{t} & \text{on } \partial\Omega_{u,N} \end{array} \tag{17}$$

where θ_D is the applied temperature on $\partial\Omega_{\theta,D}$, Q_N is the imposed heat flux on $\partial\Omega_{\theta,N}$, h is the coefficient of convective heat transfer on $\partial\Omega_{\theta,R}$, $\boldsymbol{u}_D$ is the prescribed displacement on $\partial\Omega_{u,D}$, and $\boldsymbol{t}_D$ is the applied traction on $\partial\Omega_{u,N}$.

The different portions of the surface respect the following conditions:

$$\begin{array}{l|l} \partial\Omega_{u,D} \cup \partial\Omega_{u,N} = \partial\Omega_u & \partial\Omega_{\theta,D} \cup \partial\Omega_{\theta,N} \cup \partial\Omega_{\theta,R} = \partial\Omega_\theta \\ \partial\Omega_{u,D} \cap \partial\Omega_{u,N} = 0 & \partial\Omega_{\theta,D} \cap \partial\Omega_{\theta,N} = 0 \\ & \partial\Omega_{\theta,D} \cap \partial\Omega_{\theta,R} = 0 \\ & \partial\Omega_{\theta,N} \cap \partial\Omega_{\theta,R} = 0 \end{array} \tag{18}$$

3.5. Weak formulation

Using the method of lines approach and applying a semi-implicit time integration scheme for θ in equation (7), we obtain the following weak formulation:

$$\begin{aligned} \rho c_v \int_\Omega \left(\frac{\theta - \theta^t}{dt}\right) \hat{\theta} dx - \int_\Omega \boldsymbol{q} \cdot \nabla\hat{\theta} dx - \int_\Omega Q_M^t \hat{\theta} dx \\ - \int_{\partial\Omega_{\theta,N}} Q_N \, \hat{\theta} ds + \int_{\partial\Omega_{\theta,R}} h(\theta - \theta_0)\hat{\theta} ds = 0 \end{aligned} \tag{19}$$

where θ is at the current time step, superscript t indicates quantities at the previous time step, $\hat{\theta}$ is the test function, dt is the time increment, $Q_M^t = \boldsymbol{\sigma}^t : \dot{\boldsymbol{\varepsilon}}^{p,t} - \theta\boldsymbol{\beta} : (\dot{\boldsymbol{\varepsilon}}^t - \dot{\boldsymbol{\varepsilon}}^{p,t})$ is the mechanical heat source term computed using quantities from the previous time step. Preliminary laser scanning studies showed that radiation heat loss has a negligible contribution to temperature change and hence it is disregarded here, which also makes equation (19) linear in θ and simpler to solve.

The static equilibrium equation along with the traction boundary condition yields the following weak form:

$$\int_{\partial\Omega_{u,N}} \boldsymbol{t} \cdot \hat{\boldsymbol{u}} ds - \int_\Omega \boldsymbol{\sigma} : \nabla\hat{\boldsymbol{u}} dx = 0 \tag{20}$$

where $\hat{\boldsymbol{u}}$ is the displacement test function.

3.6. Finite element (FE) implementation and algorithm

The TEVP problem is solved using a staggered approach in a FE framework. First, equation (19) is solved using a linear solver to obtain the temperature at the current time step followed by equation (20) to obtain the displacements. Due to the non-linearity in equation (20), a Newton-Raphson solver is used to solve the weak form of the governing equation,

and a second Newton-Raphson solver is used to compute the increments of internal state variables and consistent tangent operator ($\partial\boldsymbol{\sigma}/\partial\boldsymbol{\varepsilon}$) by solving the viscoplastic constitutive equation (11). The scheme is presented in Algorithm A.1 in the appendix.

The weak forms of the governing equations were numerically implemented in the open source FE library FEniCS [23] using its Python interface. The constitutive laws were implemented in MFront [24] and coupled with FEniCS using the MGIS library [25]. Simulations are performed using the Algebraic MultiGrid (AMG) preconditioners and the generalized minimal residual method (GMRES) iterative solver. In addition, if the Newton-Raphson solvers are unable to converge, a time-stepping criterion is implemented where the current time-step is divided by 2. However, if the time step is divided by more than 16 times the initial time step, then the simulation stops with a runtime error message.

4. Simulation setup

4.1. Temperature-dependent material properties

The elastic stiffness tensor is assumed to have a linear dependence on temperature [8] and this dependence is extrapolated up to the solidus temperature to get the following relationship in Voigt notation:

$$\mathbb{C}_{ij}(\theta) = \mathbb{C}_{ij}(\theta_0) + \frac{d\mathbb{C}_{ij}}{d\theta}(\theta - \theta_0) \tag{21}$$

where $\frac{d\mathbb{C}_{ij}}{d\theta}$ are constants and $i, j = 1 - 6$. The fitted parameters in equation (21) are shown in Table 1.

The temperature dependent evolutions of ρ, c_v, γ_θ and K for 316L are obtained from [26]:

$$\begin{array}{lll} \rho(\theta) & = 8084.2 - 0.42086 \times \theta - 3.8942 \times 10^{-5} \times \theta^2 & \mathrm{kg/m^3} \\ c_v(\theta) & = 458.985 + 0.13280016 \times \theta & \mathrm{J/kgK} \\ K(\theta) & = 9.248 + 1.571 \times 10^{-2} \times \theta & \mathrm{W/mK} \\ \gamma_\theta(\theta) & = 1.786 \times 10^{-5} + 2.398 \times 10^{-9} \times \theta + 3.269 \times 10^{-13} \times \theta^2 & \mathrm{K^{-1}} \end{array} \tag{22}$$

4.2. Fitting viscoplastic law and Voce hardening parameters

As mentioned in section 3.3, only dislocation glide is considered on the 12 $\{111\}\langle 110\rangle$ slip systems of the face centered cubic (austenitic) 316L. The reference shear rate $\dot{\gamma}_0$ is assumed to be constant at 1 $\mathrm{s^{-1}}$. Both self

(diagonal) and latent (off-diagonal) hardening components are set to 1 in the matrix h^{sr} (equation 14). The remainder of the viscoplastic law and Voce hardening parameters are fitted.

Fitting them requires stress-strain curves at different temperatures and at different strain-rates that are encountered during the rapid cooling that occurs in the wake of the laser scanning. Generating a reliable dataset to fit the hardening law parameters is impractical because one would need to perform hundreds of tests that encompass different temperatures (in the interval between room temperature and solidus), strain rates (corresponding to the cooling rates encountered), repeatability (at least three tests per strain rate and temperature) and two sets of samples (as-built and as-built + lasered). In lieu of these tests, the following strategy has been adopted in this work: (i) Use a temperature dependent expression for n obtained from the literature. (ii) Using the n obtained at room temperature from this formula, fit the Voce hardening parameters to obtain the stress-strain behavior at room temperature for the as-built and lasered samples studied in this work. (iii) Source experimental stress-strain curves for 316L obtained under quasi-static loading from existing literature, and use them to extract the evolution of the Voce hardening parameters as a function of temperature. (iv) Assume that the formula for n and the extracted evolution trend of the Voce hardening parameters as a function of temperature are applicable to the samples studied in this work.

A temperature-dependent power law exponent (n) formulated for FCC polycrystals by Cyr et al., [27] based on the kinetic model of Kocks [28] is chosen:

$$n(\theta) = \frac{b_B^3 \sqrt{\mu_f \times (\mu_f - \eta_f)}}{9 k_B \theta} \tag{23}$$

where b_B is the Burgers vector magnitude, $\eta_f = \mathbb{C}_{44}(\theta) + \frac{1}{2}\left(\mathbb{C}_{12}(\theta) - \mathbb{C}_{11}(\theta)\right)$ and $\mu_f = \mathbb{C}_{44}(\theta)$ are parameters related to the stiffness, and k_B is the Boltzmann constant. The evolution of n is plotted as a function of θ in Figure 2a. Another curve based on the same formula can be obtained from fitting the stress-strain curves from compression experiments for hot-rolled and annealed 316L at different temperatures performed by Puchi Cabrera [29]. However, the former curve (from [27]) is chosen for this work because comparative studies have demonstrated that AM 316L is proportionally more rate sensitive than conventionally manufactured 316L [30, 31] and this curve has a more appropriate fit. The values of b_B, k_B and θ_0 are also listed in Table 1. These values help satisfy the condition $n \geq 1$, (for $\theta < \theta_{\text{solidus}}$), which is necessary for numerical stability [32].

			$h_{met,x}$	20000	W/m^2K
			$h_{met,y}$	20000	W/m^2K
$\mathbb{C}_{11}$	204.6×10^3	MPa	$h_{met,z}$	300000	W/m^2K
$\mathbb{C}_{12}$	137.7×10^3	MPa	θ_0	300	K
$\mathbb{C}_{44}$	126.2×10^3	MPa	R_{beam}	30	µm
$d\mathbb{C}_{11}/d\theta$	-90.33	MPa	P_{beam}	24	W
$d\mathbb{C}_{12}/d\theta$	-45.10	MPa	η_{beam}	0.3	$(-)$
$d\mathbb{C}_{44}/d\theta$	-51.78	MPa	b_B	2.48×10^{-7}	mm
			k_b	1.381×10^{-23}	J/K
			q_d	10^{-3}	$(-)$
As-built zone			MZ		
$\tau_{0,AS}$	200	MPa	$\tau_{0,RF}$	520	MPa
$\tau_{1,AS}$	90	MPa	$\tau_{0,RF}$	10	MPa
$\Theta_{0,AS}$	467	MPa	$\Theta_{0,RF}$	-25	MPa
$\Theta_{1,AS}$	135	MPa	$\Theta_{0,RF}$	-165	MPa

Table 1: Material parameter (from [7]) and Voce parameter fits at 300 K (see Figure S1) for the as-built material and the MZ along with thermal boundary condition parameters from equation (17).

According to the laser scanning results presented in [4], the resolidified material in the laser-scanned zone has higher strength than the as-built material. This higher strength is attributed to the refinement of the Cr-Mo microsegregations in the MZ after laser scanning, which can be evidenced from Figure 1d. This strength difference is captured by separate fits of the Voce hardening parameters in the MZ and the as-built zone.

In order to fit the parameters for both zones, the experimental data from [4] were used. Two dogbone samples had been prepared in [4]. The first sample was produced from a polished as-built material while the second sample was procured from as-built and laser scanned material. The laser scanning was performed using a multi-pass back-and-forth strategy with 35 W laser power, 50 mm/s scan speed, 60 µm spot size and 50% overlap between consecutive scans i.e., 30 µm hatch spacing. The MZ volume fraction was found to be 0.08. The two samples had been subjected to uniaxial tension under a constant strain rate of 0.00025/s to acquire their respective stress-strain behaviors shown in Figure S1 adapted from [4].

The parameter fitting was undertaken in two stages and expedited by using the elasto-viscoplastic fast Fourier transform (EVP-FFT) numerical model used in [33] that employs identical isothermal elastic and viscoplastic

laws used in this work. In the first stage, a voxelized microstructure was created using the grain-averaged orientations acquired from the EBSD scan of the as-built sample. These data were used to fit the Voce parameters of the as-built zone using the EVP-FFT model.

In the second stage, a sandwiched voxelized microstructure was created with 92% as-built material and 8% MZ. The refined material's grain-averaged orientations for the MZ were acquired from the EBSD scan of the lasered sample. The as-built Voce hardening parameters were taken from the first stage, while those of the MZ were fitted using EVP-FFT simulations. The two fits are shown in Figure S1. The final fitted parameters for the as-built zone and the MZ at 300 K are listed in Table 1.

Note that the aforementioned multi-pass scanning (35 W, 50 mm/s, 60 µm) uses a different set of lasering parameters from the single line scan (24 W, 500mm/s, 60 µm) case studied in this work. However, backscatter electron imaging has revealed that both result in similar-sized Cr-Mo microsegregations in the MZ (see Figure S2). As the strengthening of the resolidified zone is attributed to the refinement of Cr-Mo cellular microstructure refinement, the resulting material strength is assumed to be equivalent for both cases.

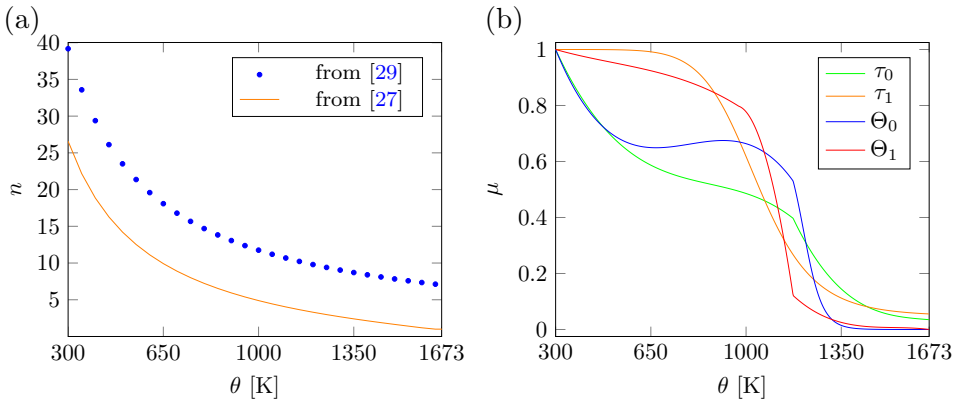

Figure 2: (a) Power law exponent n from [29] and [27] plotted as a function of θ. The orange solid curve is used in this work. (b) Multiplication factor $\mu(\theta)$ for the Voce parameters plotted as a function of θ using the data obtained from [34].

The stress-strain behavior of both the as-built and the MZ material degrades with increasing temperature. To account for this change, the Voce parameters for both zones were assumed to follow the same proportional degradation trend as that of the 316L studied in [34], leading to the fitted temperature-dependent multiplication factors $\mu(\theta)$ shown in equations (A1-

A4) and plotted in Figure 2. These factors, $\mu_{\tau_0}(\theta)$, $\mu_{\tau_1}(\theta)$, $\mu_{\Theta_0}(\theta)$ and $\mu_{\Theta_1}(\theta)$ are multiplied with their corresponding hardening parameters at room temperature (300 K) to acquire the temperature dependency. At solidus (1673 K), the hardening parameters had to be set to $(\tau_0, \tau_1, \Theta_0, \Theta_1) = (7, 5, 0, 0)$ MPa to guarantee convergence of the numerical scheme.

4.3. modelling the melt-pool and the post-melt zones

A mesh element is considered to be molten when all of its nodal temperatures are greater than or equal to the solidus (1673 K for 316L). The melt pool is a collection of all such elements in the mesh. Within a molten element, the plastic strain and cumulative slip history are erased, while the elastic stiffness tensor is reduced by three orders of magnitude ($q_d = 10^{-3}$) [7] to simulate the loss of stiffness due to melting such that:

$$\mathbb{C}_{ij}^{melt}(\theta) = q_d \, \mathbb{C}_{ij}(\theta) \tag{24}$$

Due to this reduction in stiffness, the stresses in the melt pool become negligibly small.

To account for material contraction during cooldown, the reference temperature of any element that reaches the solidus is changed from room temperature to the solidus for thermal strain calculations such that:

$$\boldsymbol{\varepsilon}^{\theta} = \boldsymbol{\gamma}^{\theta}(\theta - \theta_{solidus}) \tag{25}$$

To account for microstructure refinement in the MZ, the hardening parameters of the MZ (Table 1) are assigned to any element that exits the melt pool i.e., the temperature of at least one node of the element decreases below solidus.

Note that the mushy zone is not specifically treated in this work. Tracking the solidus and liquidus would require a much finer mesh in the melt pool than the one used in this work (see section 4.4), incurring a significantly higher computational cost that would make this simulation impractical. Furthermore, a kinetic model approximating the fraction of solid and liquid in the mushy zone is also not used in our formulation. Finally, the contribution of solidification/shrinkage strain is neglected in this work and the reasons are presented in section 6.6.

4.4. Microstructure, mesh generation and space discretization

A 3D microstructure mesh generated by extruding the 2D EBSD map of the laser scanned microstructure is chosen in this study to facilitate a one-to-one comparison between the 2D EBSD measurements and simulation

predictions; a detailed discussion on this choice is provided in section 6.1. Indeed, this procedure only allows to correctly capture the top surface of the experimentally measured microstructure. Nevertheless, as shall be seen in section 5.1, the simulations are able to provide a satisfactory match for the polar dislocation density on a statistical level.

The following procedure was used to generate the mesh. 2D EBSD data after the laser scanning was first processed using ATEX [12] for noise and spike reduction to acquire the grain averaged orientation map and grain position data. Since grain growth during solidification is not modeled in this work, the only way to account for the final grain structure is to use the EBSD data after laser scanning. A grain boundary misorientation tolerance of 5° was used to distinguish between grains. A domain of size (400 µm × 400 µm) is chosen to accommodate at least 2 layers of the as-built wall. Grain position data are then used to create an initial tetrahedral mesh using Voxel2Tet [35], which was then extruded to obtain a 2D columnar microstructure. This mesh was refined along the laser track region, and at grain boundaries, and then coarsened towards the grain centroids using MMG3D [36] to get the final mesh. Mesh convergence analysis revealed that a mesh refinement of 2.5 µm and a transitional size gradation of 2 was necessary for accuracy.

A mesh was generated using this approach for the 500 mm/s laser scan track. Simulated microstructures with two depths were analyzed, 50 µm and 100 µm, and the corresponding number of elements in the mesh were 2176649 and 5327879, respectively. With these numbers of elements, the simulations required ∼14 days and ∼64 days, respectively, for completion with 10 nodes of 40 cores each and using a time step of 10^{-6} s (section 4.7) on the Cholesky high-performance computing cluster (École Polytechnique, France). Due to limited availability of computational resources, running multiple 100 µm-depth simulations is impractical and some compromises have to be made. Beyond 50 µm, the depth does not play an important role in the formation of surface polar dislocation densities (section 5.1). However, until 100 µm, the simulated domain depth plays a role in the formation of residual stresses in the heat-affected zone. Therefore, the results presented in section 5 are those from the simulations performed using 100 µm-depth microstructure but other simulations performed for understanding the factors influencing residual state in section 5.6 have been carried out using 50 µm-depth microstructures. Figure 3a shows the final mesh for the 100 µm-depth microstructure.

The FE simulations have been performed with temperature and displacement fields approximated using polynomials of degrees 1 and 2, respectively, as a trade-off between computational cost and accuracy. Integration is per-

formed using a Gaussian quadrature of the same degree as the polynomials.

4.5. Initial conditions

In order to have a one-to-one comparison of the evolution the initial grain orientations i.e., Euler angles, were projected from the EBSD measurements of the post laser scanned sample onto the generated microstructure mesh. Once projected, the bunge convention Euler angles were used to generate the orientation tensor ($\boldsymbol{g}_{ori}(\boldsymbol{x})$) for each element in the mesh; all material points within an element were assigned the same $\boldsymbol{g}_{ori}(\boldsymbol{x})$:

$$\boldsymbol{g}_{ori}(\boldsymbol{x}) = \boldsymbol{g}(\boldsymbol{x}, \phi_1, \Phi, \phi_2) \tag{26}$$

Furthermore, as a first approximation, the initial field variables $(\boldsymbol{u}, \theta)$ were assumed to be unperturbed:

$$\begin{array}{lll} \boldsymbol{u}(\boldsymbol{x}, 0) & = (0, 0, 0) \text{ mm} & \forall \boldsymbol{x} \in \Omega \\ \theta(\boldsymbol{x}, 0) & = 300 \text{ K} & \forall \boldsymbol{x} \in \Omega \end{array} \tag{27}$$

4.6. Boundary conditions

Since the microstructure of the meshed domain is only a small portion of the microstructure in a significantly larger experimental domain, the thermomechanical boundary conditions are chosen to mimic the presence of material beyond the bounds of the meshed domain. For the mechanical boundary conditions, on the surfaces $x = 0$, $x = x_{max}$, $y = 0$, $y = y_{max}$ and $z = 0$, the normal components of the displacement field are set to zero and the complementary in-plane traction vector components are set to zero. On the surface $z = z_{max}$, a traction-free boundary condition is enforced. For the thermal boundary condition, conduction is mimicked on the surfaces $x = 0$, $x = x_{max}$, $y = 0$, $y = y_{max}$, and $z = 0$, with the help of a convective heat transfer boundary condition. The coefficients $h_{met,x}$, $h_{met,y}$ and $h_{met,z}$ in equation (19) are fitted (Table 1) to generate a temperature profile that approximately captures the width and depth of the melt pool obtained from backscatter electron images (Figure 1d) of the single pass laser-scanned cross sections from [4]. The predicted melt pool depth and width are shown in Figure S3.

Since the laser scanning has been performed in secondary vacuum, convective heat losses are not considered on the surface $z = z_{max}$. However, this surface is subjected to a Gaussian laser heat flux of the form:

$$Q_{laser}(t) = \frac{2\eta_{beam} P_{beam}}{2\pi R_{beam}^2} exp\left(2\frac{||\boldsymbol{x} - \boldsymbol{x}_c(t)||^2}{R_{beam}^2}\right) \tag{28}$$

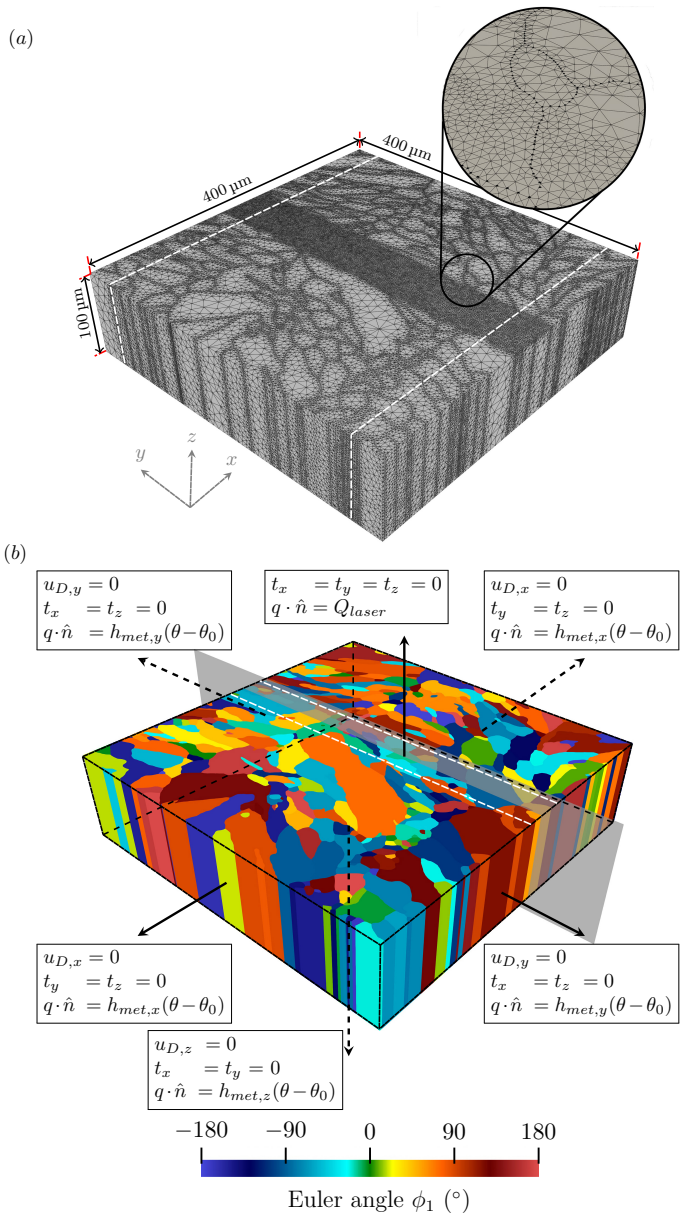

Figure 3: Setup for laser scanning simulations. (a) Final mesh for the 500 mm/s laser scan simulation with a microstructure of depth 100 µm. (b) Thermomechanical boundary conditions on each of the six surfaces of the microstructure. The grains in (b) are color-coded using the first Bunge Euler angle. The translucent plane contains the z direction and the center line of the laser scan track in the $x - y$ plane.

where η_{beam} is the absorptivity, P_{beam} is the laser beam power, R_{beam} is the radius of the beam spot, $\boldsymbol{x}$ is a point in the mesh, and $\boldsymbol{x}_c(t)$ is the position of the center of the moving laser beam. The laser scanning is simulated in such a way that when the center of the Gaussian heat source leaves the domain, it is not switched off in order to capture the temperature field when the laser is far away from the simulated domain. Figure 3b shows a schematic diagram of the applied boundary conditions over the domain.

To eliminate the influence of proximity to the domain boundaries that result in undesirable effects, a preliminary laser scanning simulation was completed assuming a single crystal microstructure. Analyzing the distribution of residual stresses and plastic strains, a region within 35 µm from both boundaries along the laser scan direction (y) is found to be influenced by the proximity to the simulated domain boundary. Consequently, the analysis is performed in a reduced region of 400 µm × 330 µm × 100 µm (demarcated by white dotted lines in Fig. 3a) to neglect boundary effects.

4.7. Time step

Finally, a time step convergence study was undertaken where laser scanning on a single crystal domain with a smaller mesh were performed, but the refinement and gradation were kept the same as those used in Figure 3a. The solutions were found to converge with the time step 10^{-6} s.

The total simulation time is 0.005 s. The laser exits the domain after 0.001 s. The simulation is stopped when the temperature in the entire domain reaches 300 K and the stress rate drops below 0.5 MPa/μs (10^{-4} times the peak stress rate during laser scanning), which takes 0.004 s.

5. Results

All the simulation results presented in this section are obtained from the simulated microstructure with 100 µm depth. The simulation videos have been provided as supplementary material.

5.1. Local and statistical comparison between simulations and experiments

The Frobenius norms of $\boldsymbol{\alpha}_{\text{exp}}$ (equation 1) computed from EBSD data with step sizes 0.5 µm and 3.0 µm, $\boldsymbol{\alpha}_{\omega^e}$ (equation 6) and $\boldsymbol{\alpha}$ (equation 5) are compared in Figure 4. The polar densities obtained with step sizes of 0.5 µm and 3.0 µm are very different in magnitude and concentrations. Therefore, only the 0.5 µm step size data is considered below. Meanwhile, both $\boldsymbol{\alpha}$ and $\boldsymbol{\alpha}_{\boldsymbol{\omega}^e}$ result in nearly the same response, which indicates that the

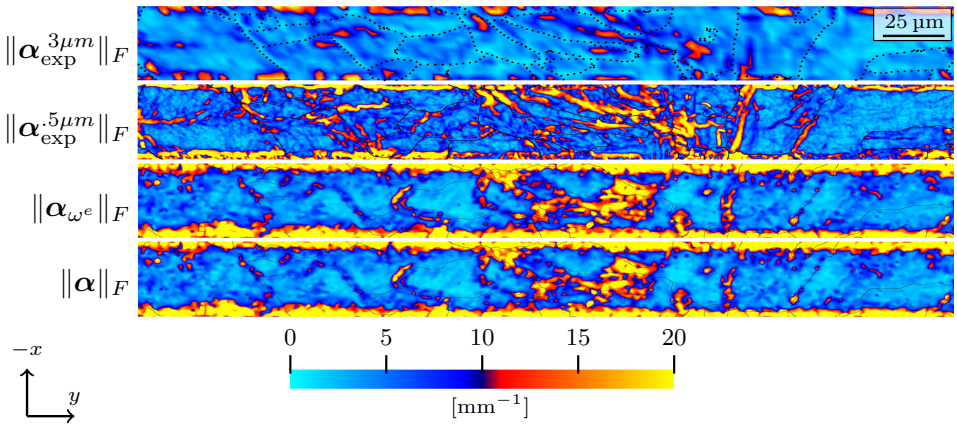

Figure 4: The TEVP-FE simulation predicted polar dislocation density in the MZ in comparison with the experimentally measured ones. To facilitate this comparison, the Frobenius norms of $\boldsymbol{\alpha}_{\text{exp}}$ (equation 1) computed from EBSD data with step sizes 0.5 µm and 3.0 µm, $\boldsymbol{\alpha}_{\omega^e}$ (equation 6) and $\boldsymbol{\alpha}$ (equation 5) for the 500 mm/s laser scan using the 100 µm-depth microstructure are computed and compared. The contour plot color scheme has been capped at 20 mm^{-1} to facilitate a qualitative comparison. A quantitative comparison is presented in Figure 5.

contribution of heterogeneously distributed $\boldsymbol{\omega}^e$ (due to plastic deformation) to $\boldsymbol{\alpha}$ is significantly more important than that of $\boldsymbol{\varepsilon}^e$.

Due to the experimental errors, model assumptions and interpolations to compare data (appendix A.4), a reasonably good match is obtained but only at some locations between the experimental (with 0.5 µm step size) and simulated polar dislocation densities. A high concentration of $\|\boldsymbol{\alpha}\|_F$ can be observed all along the edges of the MZ in the experimental measurements, indicating that there is a significant concentration of plastic deformation along these edges. Importantly, this density concentration is well captured by the simulations; this shall become evident in section 5.2. Furthermore, the model-predicted densities exhibit a heterogeneous distribution not only at the grain boundaries but also inside the grains.

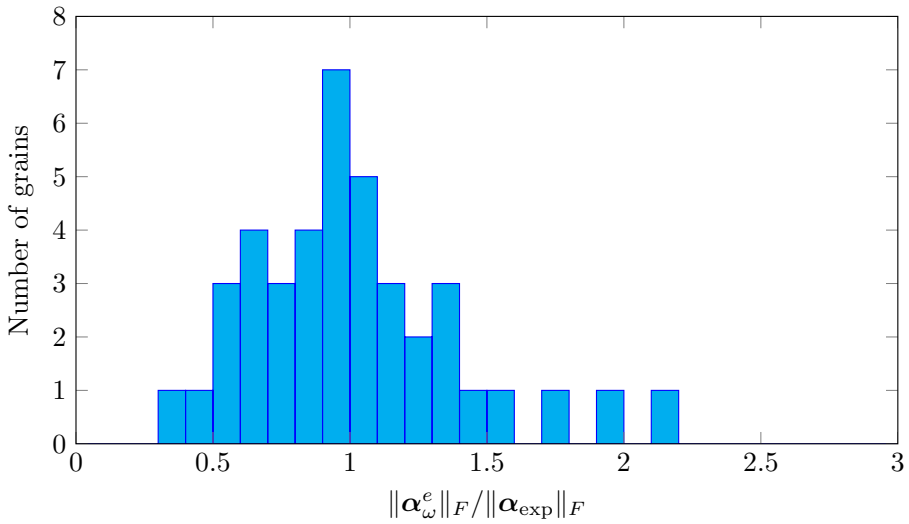

Figure 5: Histogram of the ratio of the Frobenius norms of the grain surface-averaged $\boldsymbol{\alpha}_{\omega^e}$ and $\boldsymbol{\alpha}_{\text{exp}}$ for all the grains along the MZ.

However, at most locations within the MZ, simulations do not correctly capture the localization and a pointwise quantitative comparison with measured densities would yield significant differences. However, a more reasonable comparison can be performed after a judicious statistical averaging of the polar densities. To that end, the ratio of the Frobenius norms (equation A5) of the grain surface-averaged partial polar dislocation density predicted by the model and the ones experimentally measured are plotted in Figure 5; the grain surface averaging is performed after computing the Frobenius norm and using all the elements/pixels belonging to a grain on the top surface of the domain along the MZ; see Appendix A.4 for more details.

There are 41 grains in the studied portion of the MZ. For all the grains, the ratio $\|\boldsymbol{\alpha}^e_\omega\|_F/\|\boldsymbol{\alpha}_{\text{exp}}\|_F$ falls between 0.3 and 2.2. Furthermore, for 38 grains, this ratio is between 0.5 and 2, and for 12 grains, it is between 0.9 and 1.1. Therefore, the simulation predicted densities have a much better quantitative match with the experimental densities from a grain surface-average standpoint than from a local standpoint.

In what follows, the results on the stress and plastic strain evolution during scanning will be presented from a qualitative standpoint with the help of contour plots; this analysis will help understand the extent to which the stresses and plastic strains propagate into the domain. Then, a quantitative

analysis is performed either for the grain surface-averaged values in the residual state or from a local standpoint in comparison to other simulations.

5.2. Temperature and thermal strain evolution

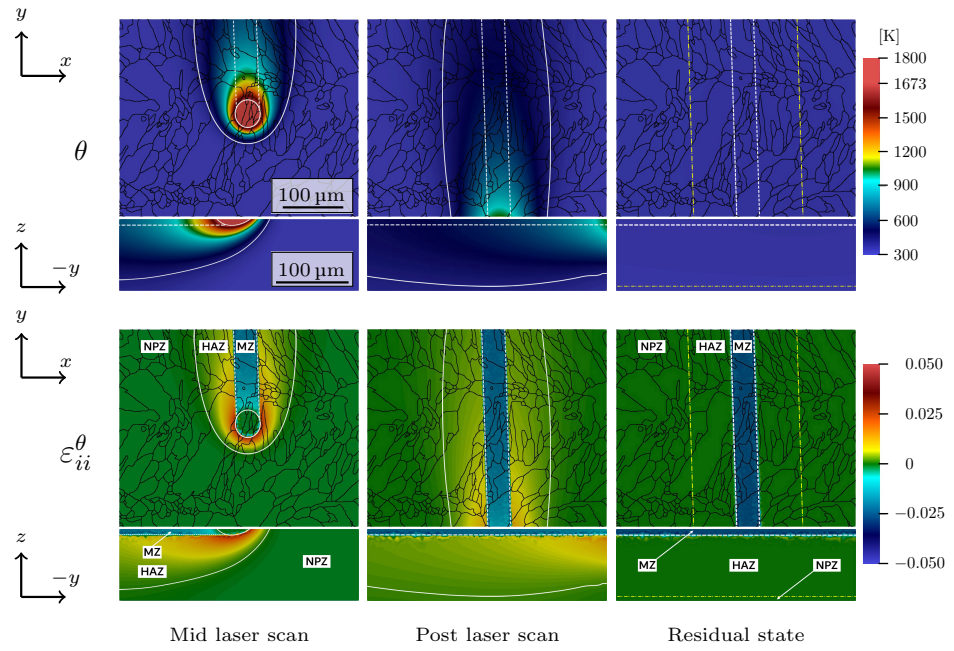

Figure 6: Temperature and thermal strain evolution and determining MZ, HAZ and NPZ. Top and cross sectional views (according to Figure 3) of the temperature and thermal strain components $ii = xx,\ yy,$ or zz when the laser is midway during scanning (Mid laser scan), just left the domain at the bottom (Post laser scan) and at the end of the simulation (Residual state) are shown. The dotted white lines demarcates the MZ. The solid white lines bound the HAZ during scanning. The dotted-dashed yellow line in the residual state maps demarcate the region where the temperature reached as high as 400 K during laser scanning i.e., the largest extent of the HAZ. One scale is used for all the top view and another one for all the cross-sectional view plots. Both scales are shown in the top left image set.

Snapshots of the temperature and thermal strain evolution at different time steps: (i) when the laser is nearly at the middle of the domain, (ii) when the laser has just left the domain, and (iii) in the residual state when the temperature in the domain has reduced to the reference temperature, are shown in Figure 6. Negative thermal strain components $\varepsilon^{\theta}_{xx}$, $\varepsilon^{\theta}_{yy}$ and $\varepsilon^{\theta}_{zz}$ are generated according to equation (25) in the wake of the melt pool i.e., in the MZ (Figure 6). The MZ is surrounded by the heat affected zone

(HAZ), which is defined as the region where $\theta \in [400\text{ K}, 1673\text{ K})$; as shall be seen in the following sections, plastic deformation is concentrated in the HAZ. Furthermore, in the HAZ, $\varepsilon^{\theta}_{xx}$, $\varepsilon^{\theta}_{yy}$ and $\varepsilon^{\theta}_{zz}$ are positive. The region where θ is less than 400 K is denoted as the negligible plasticity zone (NPZ) where (as shall be seen in section 5.4) plastic strains of magnitudes less than 0.0001, and often equal to 0, occur. Note also that in the residual state, the HAZ bounds the region where the nodal temperatures reached as high as 400 K during the entire laser scanning.

As the laser leaves the simulated microstructure and the temperature reduces to room temperature, only the negative thermal strains remain in the MZ; in the remainder of the microstructure, they reduce to zero. Note that the thermal strain profile is not affected by the elastic and plastic anisotropy and heterogeneity of the 316L polycrystal.

5.3. Stress evolution

According to equation (9) and the temperature gradient mechanism [37], the MZ with its negative thermal strains should result in strong tensile in-plane normal stress components on the traction-free (top) surface and underneath it, which is indeed the case as seen for σ_{xx} and σ_{yy} in Figure 7. In addition, the portion of the HAZ with strongly positive thermal strains occurring just ahead and on the sides of the melt pool results in strong compressive stresses, which can also be deduced from equation (9). In the wake of the melt pool, the HAZ also has positive thermal strains, but their magnitudes are lower, whereas the magnitudes of the negative thermal strains increase with the distance away from the melt pool. Consequently, the tensile σ_{xx} and σ_{yy} decrease in magnitude along x and z in the wake of the melt pool and away from the MZ until zero σ_{xx} and σ_{yy} surfaces are formed inside the HAZ. These surfaces start from the melt pool and extend in its wake separating the strong tensile region from the compressive one. A second set of zero σ_{xx} and σ_{yy} surfaces emerge in front of the compressive region in the NPZ and extend in all directions of the domain. As the laser continues scanning and leaves the simulated zone, the second set of zero σ_{xx} and σ_{yy} surfaces are swept away causing almost every material point in the microstructure to experience an initial compression. However, this is rapidly followed by the widening and deepening of the first zero σ_{xx} and σ_{yy} surfaces causing most material points in the top half of the simulated domain to experience tensile σ_{xx} and σ_{yy} in the residual state.

Meanwhile, since the top surface has traction free boundary conditions, σ_{zz} (along with σ_{xz} and σ_{yz}) is zero on that surface. However, it is non-zero underneath this surface, which can be deduced from equation (9). At the

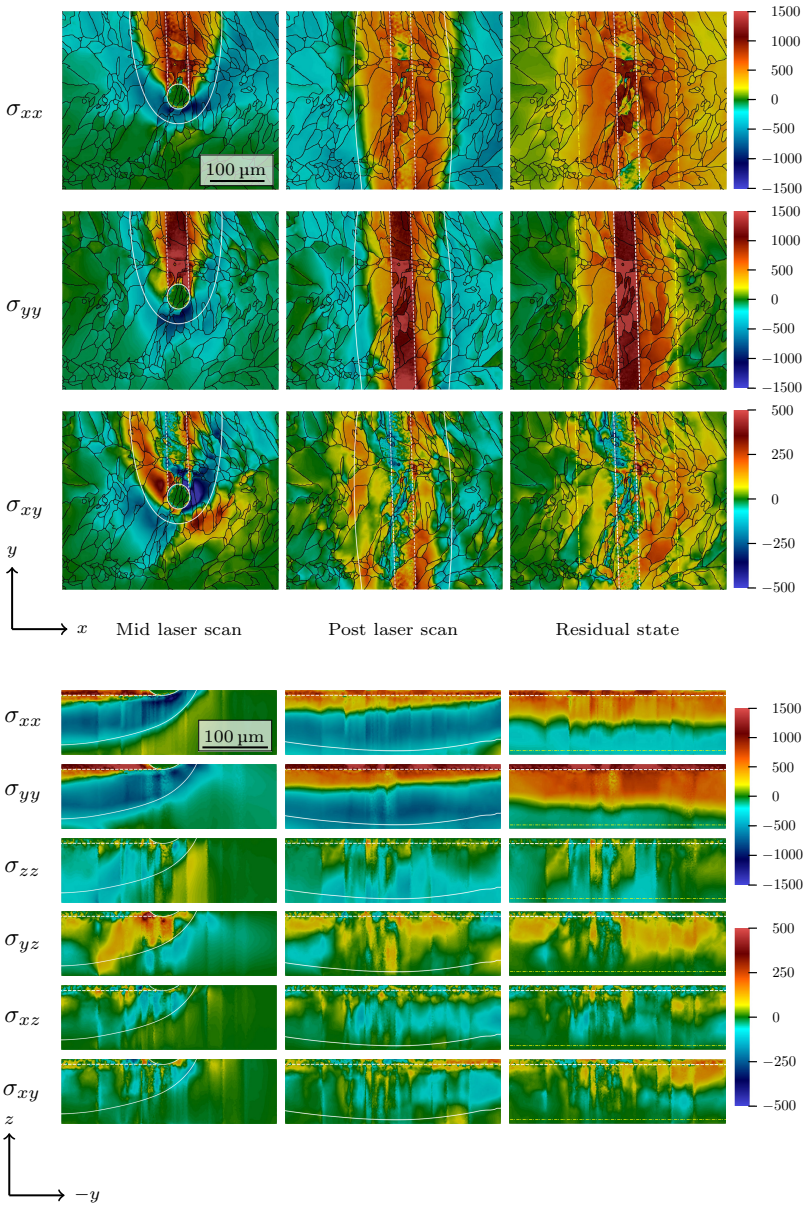

Figure 7: Non-zero stress components (MPa) on the top and cross-sectional (from Figure 3b) surfaces at the mid laser scan, post laser scan and residual states defined in Figure 6. The dotted-dashed yellow lines in the residual state maps demarcate the region where the temperature reached as high as 400 K during laser scanning i.e., the largest extent of the HAZ. Stress magnitudes in contour plots have been capped at 1.5 GPa for visualization.

border between MZ and HAZ, a tensile σ_{zz} zone is generated that extends deeper beyond the melt pool depth. Further below in the HAZ, however, σ_{zz} is compressive and remains compressive until the bottom surface.

The shear stress σ_{xy} $(= \sigma_{yx})$ manifests on the top surface and the studied cross-section but its highest magnitude is three times lower than that of σ_{xx} and σ_{yy}. Due to the laser passage, the material ahead of the melt pool is pushed/dragged along the $-y$ direction whereas the surrounding material tends to resist this motion. As a consequence, a positive and negative σ_{yx} is generated in the HAZ behind the melt pool on its left and right, respectively. However, the force exerted along y in the wake of the melt pool results in the formation of negative and positive σ_{yx} in the vicinity of the left and right boundaries, respectively, of the MZ. Meanwhile, ahead of the melt pool, in the HAZ and the NPZ, negative and positive σ_{yx} is generated to the left and right portions of the domain, respectively. In the HAZ and NPZ underneath the melt pool, respectively, negative and positive σ_{yx} are generated.

Since $t_x = t_y = 0$ on the top and bottom surfaces, σ_{xz} $(= \sigma_{zx})$ and σ_{yz} $(= \sigma_{zy})$ are both equal to 0 on these surfaces. However, they evolve between these surfaces. In the studied cross section, they tend to be generally positive in the HAZ and zero or negative in the NPZ.

5.4. Plastic strain evolution

Interestingly, a strong positive ε^p_{xx} is generated starting at the interface between the MZ and the HAZ and extending slightly into the HAZ from the beginning of laser scanning until the residual state as seen in Figures 8 and 9. This high concentration zone is surrounded by a wider and deeper negative ε^p_{xx} zone that manifests stronger in the HAZ than in the MZ. In fact, the MZ ends up having negative ε^p_{xx} only in a small portion in the vicinity at the end of the simulation. Meanwhile, ε^p_{yy} is positive inside the MZ, zero at the interface between the MZ and the HAZ, and negative in the HAZ along both x and z directions. Since plastic deformation does not result in any volume change, the evolution of ε^p_{zz} is the same as $-\varepsilon^p_{yy} - \varepsilon^p_{xx}$ as can be deduced from Figures 8. Since the concentrations of ε^p_{xx} and ε^p_{yy} do not occur at the same locations in the domain, the highest magnitude of ε^p_{zz} coincides with that of ε^p_{xx}. This high concentration of plastic strain components at the border between MZ and HAZ is accompanied by a high concentration of plastic rotations in the same region, which contributes to the polar dislocation density concentrations shown in Figure 4.

Similar to σ_{xy}, alternating positive and negative (and vice versa) profile of ε^p_{xy} occurs in the HAZ to the left (and right) of the MZ. In the cross

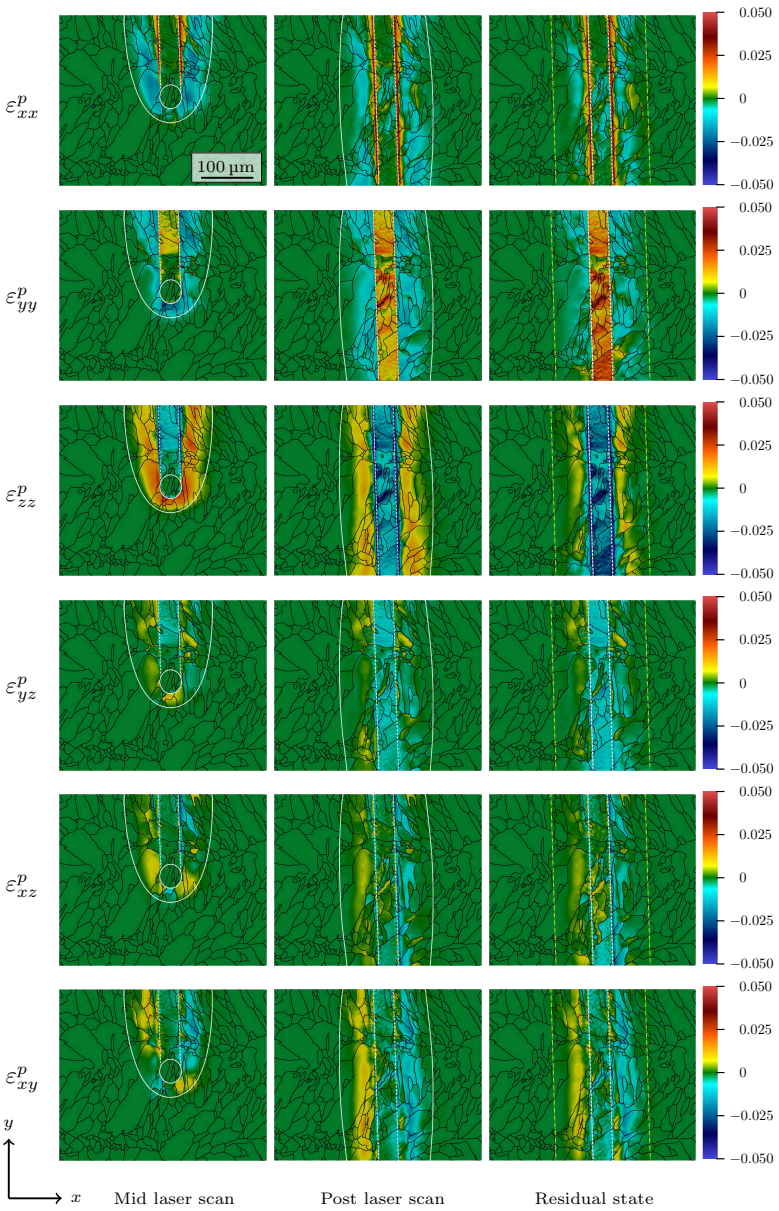

Figure 8: Plastic strain components on the top surface at the mid laser scan, post laser scan and residual states defined in Figure 6. The dotted-dashed yellow line in the Residual state maps demarcate the region where the temperature reached as high as 400 K during laser scanning i.e., the largest extent of the HAZ.

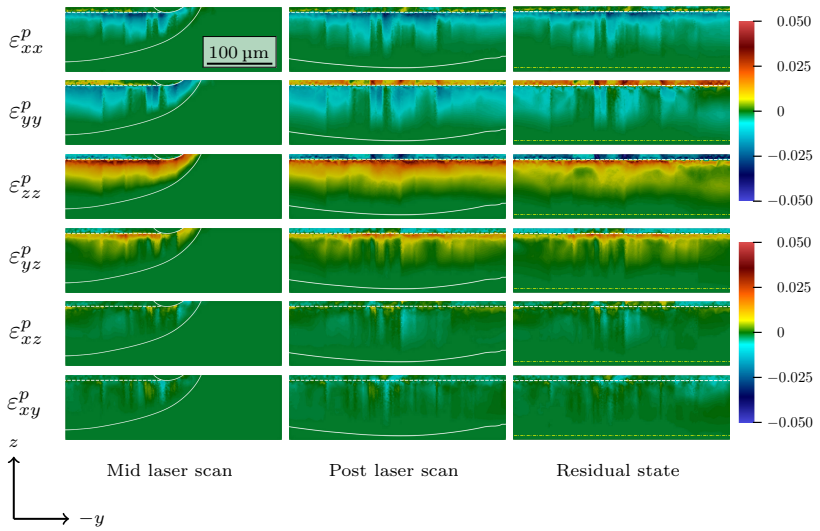

Figure 9: Plastic strain components on the cross-sectional surface (from Figure 3b) at the mid laser scan, post laser scan and residual states defined in Figure 6.

section, however, it is primarily negative. The evolution of ε^p_{xz} is quite similar to that of ε^p_{xy} in the studied cross-section.

5.5. Residual stresses and plastic strains - a quantitative analysis

The strongest stress and plastic strain magnitudes manifest after the material has cooled down to the reference temperature 300 K everywhere in the domain i.e., in the residual state. The highest magnitudes of σ_{xx} and σ_{yy} occur in some grains within the MZ. σ_{xx} is spread into both HAZ and NPZ much farther along x than σ_{yy}. However, σ_{yy} spreads deeper into the HAZ along z than σ_{xx}. Both σ_{xx} and σ_{yy} are tensile in the NPZ on the top surface but compressive in the NPZ underneath. Meanwhile, the shear stress σ_{xy} has the highest magnitude at the border of the MZ and the HAZ. The highest and lowest values of σ_{xz}, σ_{yz} and σ_{zz} occur in the HAZ underneath the MZ.

Unlike the spread in the stress components, the plastic strain components are confined primarily within the MZ and the HAZ; they spread on either side of the MZ nearly the same distance along x as the width of the MZ and they penetrate a little more than half the depth of the domain.

The thermal strains clearly have a more dominant effect on the spread of the residual stresses and plastic strains than the elastic anisotropy and plastic heterogeneity. As seen in Figure 7, one large grain to the left of the MZ experiences a strong gradient in σ_{yy} and σ_{xy} along x. Nevertheless, the

elastic and plastic anisotropy and heterogeneity result in non-uniform stress and plastic strain distribution and play an important role in determining their magnitudes. This is further explored in section 5.6.

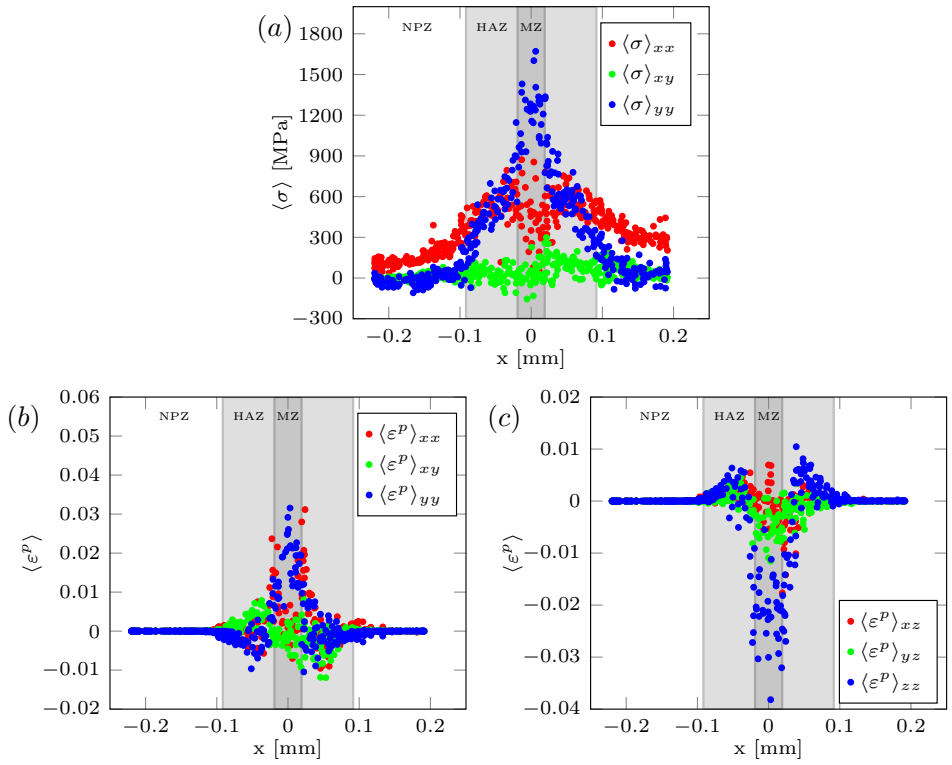

Figure 10: Grain surface-averaged residual stress and plastic strain components plotted as a function of the distance along x from the center of the laser scan path. The laser path subtends an angle of 1.86° with respect to y, hence the x distance of grain centroids with respect to the center line of the laser path is not symmetric about 0. The residual state MZ and HAZ are demarcated using grey shaded regions.

To better quantify the spread in residual stress and plastic strain components, their grain surface-averaged values $\langle\sigma_{ij}\rangle$ (i.e., averaged on the top surface of a grain) are plotted as a function of the distance along x from the center of the laser scan path in Figure 10; as mentioned at the end of section 5.1, the simulation-predicted grain surface-averaged quantities are more reliable than the local ones and hence the former are studied quantitatively. The results clearly show that the lasering affects stresses all the way to the boundaries of the domain along x but the plastic deformation is primarily confined in the MZ and the HAZ, in a region $\pm 100\,\mu$m from the center line

of the laser scan path. The variation between the stresses and plastic strain components at a fixed distance from the center of the laser scan line is the highest within the MZ and gradually diminishes away from this line until the edges of the HAZ. For some grains within the MZ, $\langle \sigma_{yy} \rangle$ reaches as high as ~ 1.7 GPa, whereas the highest $\langle \boldsymbol{\varepsilon}^p_{xx} \rangle$ and $\langle \boldsymbol{\varepsilon}^p_{yy} \rangle$ are ~ 0.03, and the lowest (highest magnitude of) $\langle \boldsymbol{\varepsilon}^p_{zz} \rangle$ is ~ -0.04; this occurs due to the higher yield strength of the MZ (see Table 1). Meanwhile, the shear stress $\langle \sigma_{xy} \rangle$ does not exceed 300 MPa, which is found in the MZ, whereas all the grain surface-averaged plastic shear strains are confined within $\pm$ 0.02.

5.6. Impact of MZ strengthening and elastic and plastic anisotropy on the residual state

Surface laser scanning is known to produce in-plane tensile residual stresses on the MZ [38, 39] and compressive stresses underneath the MZ [40, 41]. These results are reproduced by the simulations. In this section, the role of strengthening of the MZ due to microstructure refinement, elastic anisotropy and plastic heterogeneity on the residual stress and plastic strain magnitudes and distribution is studied.

As mentioned in section 4.4, due to limited computational resources, the simulations in this section are run using simulated microstructures of 50 µm depth and all comparisons are performed with these microstructures. The comparison between the stresses and plastic strains predicted for the 500 mm/s case using the 50 µm and 100 µm depth is shown in Figure S5. The differences primarily occur for the stress fields in the NPZ, where the magnitudes are much lower than those in the MZ and HAZ. However, these differences do not preclude the comparisons that are conducted below.

Figure 11a shows the results of the simulation conducted with the 50 µm depth with the exact same model parameters as those used for the 100 µm depth simulation studied thus far. In what follows, these results shall be used as the basis to understand the role of MZ strengthening, elastic anisotropy and plastic heterogeneity.

5.6.1. Role of MZ strengthening

In this section, the effect of using the stronger resolidified material due to cellular microstructure refinement caused by laser scanning [4] is discussed. To that end, the 500 mm/s laser scan case is re-run but without changing the Voce hardening parameters (Table 1) in the MZ i.e., the same parameters as those of the as-built material are used, and the residual stress and plastic strain states are compared.

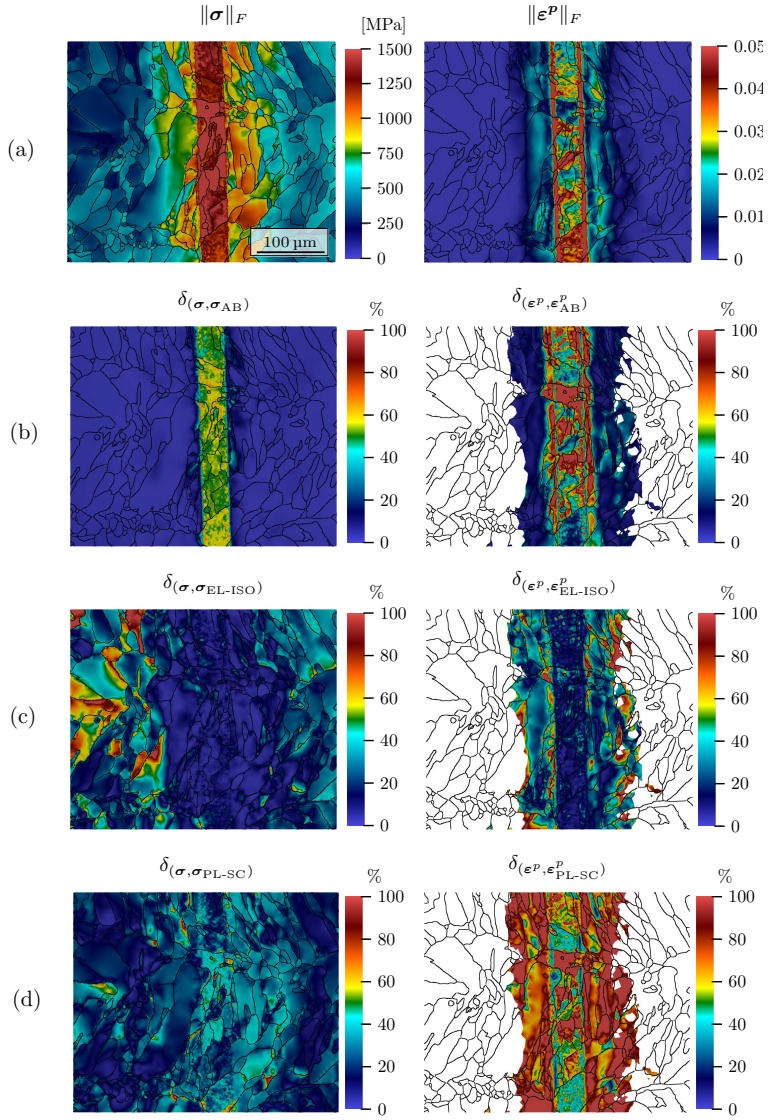

Figure 11: Understanding the roles of microstructure refinement, elastic anisotropy and plastic heterogeneity on residual stress and plastic strain formation. (a) Frobenius norms $\|\boldsymbol{\sigma}\|_F$ and $\|\boldsymbol{\varepsilon}^p\|_F$ for the 500 mm/s simulation accounting for the strengthening effect due to microstructure refinement in the MZ but simulated on a microstructure with 50 µm depth. (b) $\delta_{(\boldsymbol{\sigma},\boldsymbol{\sigma}_{\mathrm{AB}})}$ (left) and $\delta_{(\boldsymbol{\varepsilon}^p,\boldsymbol{\varepsilon}^p_{\mathrm{AB}})}$ (right) from section 5.6.1. (c) $\delta_{(\boldsymbol{\sigma},\boldsymbol{\sigma}_{\mathrm{EL\text{-}ISO}})}$ (left) and $\delta_{(\boldsymbol{\varepsilon}^p,\boldsymbol{\varepsilon}^p_{\mathrm{EL\text{-}ISO}})}$ (right) and (d) $\delta_{(\boldsymbol{\sigma},\boldsymbol{\sigma}_{\mathrm{PL\text{-}SC}})}$ (left) and $\delta_{(\boldsymbol{\varepsilon}^p,\boldsymbol{\varepsilon}^p_{\mathrm{PL\text{-}SC}})}$ (right) from section 5.6.2. For (b), (c) and (d) the $\boldsymbol{\sigma}$ and $\boldsymbol{\varepsilon}^p$ correspond to the ones used in (a). For the $\delta_{(\boldsymbol{\varepsilon}^p,\boldsymbol{\varepsilon}^p_{\mathrm{AB}})}$, $\delta_{(\boldsymbol{\varepsilon}^p,\boldsymbol{\varepsilon}^p_{\mathrm{EL\text{-}ISO}})}$ and $\delta_{(\boldsymbol{\varepsilon}^p,\boldsymbol{\varepsilon}^p_{\mathrm{PL\text{-}SC}})}$ maps, the contour plots are limited to the region where $\|\boldsymbol{\varepsilon}^p\|_F \geq 0.01 \cdot \max\left(\|\boldsymbol{\varepsilon}^p\|_F\right)$. Note that all the data have only been taken from the top surface. Scale bars for the errors have been capped at 100% to facilitate visualization.

In order to facilitate the comparison, the following measure is computed:

$$\delta_{(\boldsymbol{A},\boldsymbol{B})} = 100 \cdot \frac{\|\boldsymbol{A} - \boldsymbol{B}\|_F}{\|\boldsymbol{A}\|_F} \tag{29}$$

where $\boldsymbol{A}$ and $\boldsymbol{B}$ are two second order tensors.

Figure 11b shows $\delta_{(\boldsymbol{\sigma},\boldsymbol{\sigma}_{AB})}$, where $\boldsymbol{\sigma}$ and $\boldsymbol{\sigma}_{AB}$ are the stresses from the simulations with the MZ having respectively the modified (Figure 11a) and as-built Voce hardening parameters. Figure 11b also shows $\delta_{(\boldsymbol{\varepsilon}^p,\boldsymbol{\varepsilon}^p_{AB})}$, where $\boldsymbol{\varepsilon}^p$ and $\boldsymbol{\varepsilon}^p_{AB}$ are the plastic strains for the aforementioned simulations computed in the region of the top surface that has $\|\boldsymbol{\varepsilon}^p\|_F \geq 0.01 \cdot \max\left(\|\boldsymbol{\varepsilon}^p\|_F\right)$.

For the stress field, the differences occur mainly inside the MZ with the measure $\delta_{(\boldsymbol{\sigma},\boldsymbol{\sigma}_{AB})}$ greater than or equal to 50% and reaching up to ∼70% at some locations. Meanwhile, the most striking differences arise in the case of $\delta_{(\boldsymbol{\varepsilon}^p,\boldsymbol{\varepsilon}^p_{AB})}$, where this measure at many locations inside the MZ, in the HAZ and in its immediate vicinity experience a difference of more than 100%, and one node even attains a value of 630%.

5.6.2. Role of elastic anisotropy

To study the role of elastic anisotropy, the 50 µm depth simulation accounting for strengthening due to microstructure refinement is re-performed assuming elastic isotropy (EL-ISO) with Young's modulus of 200 GPa and Poisson's ratio of 0.3. Plastic anisotropy and heterogeneity are kept intact in the simulation. Therefore, grain orientations only affect the plastic response. The quantities $\delta_{(\boldsymbol{\sigma},\boldsymbol{\sigma}_{\text{EL-ISO}})}$ and $\delta_{(\boldsymbol{\varepsilon}^p,\boldsymbol{\varepsilon}^p_{\text{EL-ISO}})}$ are computed and plotted in Figure 11c. Interestingly, elastic isotropy has nearly no effect on the residual stresses in the MZ and the HAZ but significant differences (greater than 100%) occur in the NPZ, where elastic deformation dominates. Meanwhile, the predicted plastic strains are similar in the MZ but demonstrate stronger variations in the HAZ.

5.6.3. Role of plastic heterogeneity

The role of plastic heterogeneity is studied by re-performing the 50 µm depth simulation accounting for strengthening due to microstructure refinement while maintaining the elastic anisotropy of 316L but the entire microstructure is assumed to be plastically a single crystal (PL-SC) with the Euler angles in Bunge convention being $(0, 0, 0)$. The quantities $\delta_{(\boldsymbol{\sigma},\boldsymbol{\sigma}_{\text{PL-SC}})}$ and $\delta_{(\boldsymbol{\varepsilon}^p,\boldsymbol{\varepsilon}^p_{\text{PL-SC}})}$ are computed and plotted in Figure 11d. The assumption of plastic homogeneity results in significant differences in the entire microstructure; in particular, the stress differences are high in the MZ and the HAZ, whereas the plastic strain differences are the highest in the HAZ.

6. Discussion

6.1. Generating synthetic 3D microstructures for a one-to-one comparison

It is clear that in order to better predict the stress and plastic strain evolution under the action of laser scanning and to obtain a better match with experimental observations, the simulated 3D domain must be as close to the experimental 3D microstructure as possible. In spite of this well known fact, the 3D mesh used in this work was generated from a 2D EBSD microstructure through an extrusion process resulting in 2D columnar grains, as seen in section 4.4. There are several possibilities to generate synthetic 3D microstructures and we have described below why some of them can be impractical and others would not provide a better comparison.

State-of-the-art synthetic microstructure generators such as Neper [42], Dream3D [43], MCRpy [44], etc., take the 2D EBSD microstructure as input to generate 3D microstructures that are statistically representative of the original microstructure. However, this precludes a one-to-one comparison. Another possibility would be to generate such microstructures from solidification simulations using techniques based on phase field [8, 45], cellular automata [46, 47], kinetic Monte Carlo [48, 49], etc. However, performing such simulations on domains $\sim 400 \times 400 \times 100\,\mu m^3$ is computationally very costly and there is no guarantee that the predictions are able to accurately predict the grain structure in the depth, even in the case of the large-scale phase-field solidification model [45]. The closest that one could approach to the 3D experimental microstructure is to use the TriBeam technolody [50] based 3D EBSD, but this method is still not widely available and currently impractical from the point of view of accessibility and time to reconstruct polycrystalline microstructures of the order of $\sim 400 \times 400 \times 100\,\mu m^3$ needed for this work. The final possibility would be to generate non-AM microstructures using e.g., Voronoi tessellations. However, a quantitative analysis performed on any such microstructures would not translate to the experimental microstructure studied in this work due to the latter's unique grain morphology obtained during the AM process and after laser scanning. Arguably, 2D extruded and Voronoi tesselated microstructures would be similar in their incorrectness.

Naturally, the heterogeneity in stress and plastic strain distribution is entirely lost in the depth, and up to a certain extent on the top surface, when simulating a 2D extruded domain (extruded in the depth). Nevertheless, the average extent to which the intergranular residual stresses and plastic strains extend into the domain away from the melt pool should not

be significantly affected because these depend primarily on domain sizes and boundary conditions.

6.2. Setting the benchmark for experiment-simulation comparison

Due to the simplicity of the small deformation-based TEVP-FE model with isotropic hardening and the 2D extruded nature of the simulated microstructure, the simulations are only able to appropriately capture the concentration of polar dislocation densities at a few locations in the MZ (Figure 4). However, from a statistical standpoint, a much better match is obtained. Specifically, the grain surface-averaged Frobenius norm of the simulation predicted partial polar dislocation densities (equation 6), $\|\boldsymbol{\alpha}^e_\omega\|_F$, lies within one order of magnitude of $\|\boldsymbol{\alpha}_{\text{exp}}\|_F$ for all the grains in the MZ. Furthermore, $\sim 93\%$ of these grains exhibit a maximum factor of 2 difference (higher or lower), and $\sim 29\%$ fall within a 10% difference.

In the context of laser scanning and metal AM, it is the first time that such a one-to-one comparison between experiments and simulations has been attempted, and this work sets the benchmark for any such comparisons in the future. For those researchers who could be interested in comparing their simulation results against this benchmark, the 2D EBSD data before and after laser scanning and the 3D mesh used in this work have been made available in the supplementary material.

An important difference between the simulations performed in this work with respect to those in [5, 8, 10] arises from the treatment of the melt pool and the change in the reference temperature in the wake of the laser. The change in the reference temperature, generates a discontinuity between the thermal strains of the MZ and the HAZ, leading to significant transverse plastic strains (ε^p_{xx}) along the track boundary. This localization results in the generation of polar dislocation densities along the interface between MZ and HAZ, which are also observed in the EBSD measurements (Figure 4). This localization has not yet been reported in the literature and the match with the experiments validates the assumption made for the change in the reference temperature as well as the erasure of plastic deformation history inside the melt pool.

6.3. Tradeoff between domain size and incorporating more physical phenomena into the model

This study shows that the domain size plays a significant role in determining the residual stresses and plastic strains. For the studied case, it is found that a ratio of $1 : 16.2$ between the melt pool depth and domain depth, and a ratio of $1 : 5.6$ between the melt pool width and domain width were

necessary to appropriately capture the extent to which the laser scanning affects the stresses. Furthermore, figure S5 shows that a change in the ratio of melt pool to domain depth from 1:16.2 to 1:8.1, results in overestimating the magnitude of grain surface-averaged σ_{xx} and σ_{yy} by a factor of 2 in the NPZ in addition to the variation of plastic strain in the MZ, HAZ and NPZ.

Other simulations [5, 7, 8] studying residual stress and plastic strain formation during AM have focused either on capturing multi-physical behavior (thermo-fluid dynamics and grain growth) or on incorporating a large deformation formulation. However, in all of these works, even for the case of the shallowest and thinnest melt pools, the ratios between melt pool depth/width and domain depth/width are much greater than the ones studied in this work and altering the domain sizes would certainly alter the stress and plastic strain magnitudes and distribution.

Irrespective of the amount of physical phenomena incorporated into the model, the domain size must be sufficiently large that a further increase does not significantly affect the stress and plastic strain formation. Furthermore, it must be accompanied with appropriate boundary conditions and reference temperature selection.

6.4. Stress and plastic strain evolution during laser scanning

It is clear that the domain size and boundary conditions have a strong effect, and the (2D extruded or 3D) nature of microstructure has a lesser effect, on the average extent to which the stresses and plastic deformation propagate into the domain and their magnitudes; naturally, local variations in stresses and plastic strains would change depending on the nature of the simulated microstructure. The independence of the general trend in the evolution of stress and plastic strain components from the nature of the microstructure is visible in Figures 7, 8 and 9. The highest stress and plastic strain magnitudes are encountered for the normal component along the laser scanning direction y. However, while σ_{yy} penetrates the deepest in the domain, it is the stress component σ_{xx} that extends the farthest in the in-plane transverse direction x.

Neither these trends, nor the consequences of having a shorter melt pool to domain size ratio on these trends and magnitudes, have been reported in other related studies [5, 8].

6.5. Role of MZ strengthening, elastic anisotropy and plastic heterogeneity on the residual state

The laser scanning had resulted in a change in the intragranular cellular solute segregation structures causing the MZ to have a hybrid microstruc-

ture; due to the faster cooling rates obtained during the post-process lasering, the MZ had an order of magnitude smaller Cr-Mo segregations in comparison to the as-built material (see Figure 1b, c). This refinement changes the plastic properties locally, causing an increase in strength. If this increase in strength is neglected, then the residual stress state is underestimated by nearly a factor of 2 and the plastic strain in the residual state is overestimated by more than 100% (see Figure 11b). However, these differences are localized only in the MZ and its border with the HAZ; the change in strength has a negligible effect in the HAZ and NPZ. Nevertheless, it is clear that the strengthening (or weakening) contribution must be accounted for whenever a microstructural evolution (in the form of intragranular or grain structure change) is being simulated in which case a hybrid microstructure would be obtained. To the best of our knowledge, such considerations have never been taken into account in other works [7, 8, 10] in spite of the fact that laser scanning and grain growth simulations have been performed, which should result in strength differences between the MZ and the surrounding/reference material.

Meanwhile, neglecting elastic anisotropy results in almost no difference in the residual stress state in the MZ and the HAZ but significant differences arise in the NPZ (see Figure 11c). Furthermore, differences in plastic strains occur mainly in the HAZ. Whereas plastic heterogeneity plays a more significant role in the MZ and the HAZ in determining both the residual stresses and plastic strains (see Figure 11d). Putting these results together, it is clear that both elastic anisotropy and plastic heterogeneity are crucial to capture the intergranular stress and plastic strain distributions but in different regions of the domain.

6.6. Roadmap to improve the match between predictions and measurements

From a modelling standpoint, there is certainly room for improvement and the manner in which the comparison is performed with experiments. A 3D grain morphology and evolution should play an important role and should be incorporated whenever possible. However, this requires obtaining information using 3D techniques such as 3D EBSD, diffraction contrast tomography, etc., or predicted from solidification simulations. Information on the residual stresses in the initial microstructure could be crucial to predict the residual stress and plastic strain response, in particular in the HAZ and NPZ. Strain gradient plasticity or higher order continuum models may become important to better predict slip trace appearance correctly. Evolution (including transport) of dislocation ensembles (both statistical and geometrically necessary) needs to be considered [16, 51]. Temperature-dependent

dislocation density evolution-based hardening laws will need to be developed and incorporated into the model to better capture the single crystal plastic response at a material point. Melt pool dynamics would need to be treated using coupling with computational fluid dynamics to better capture the temperature distribution in the system. For multiple laser scans, a large deformation framework may be necessary. In addition, a parameter sensitivity analysis must be conducted prior to adding more physics, which often incurs a significantly high computational cost. Importantly, the viscoplastic constitutive law and the hardening law would have to account for strain path change effects. The contribution of shrinkage strains to plastic deformation was recently addressed in the context of AM in [14] and may need to be considered.

It has been shown that not accounting for the aforementioned aspects nevertheless leads to a reasonably good and quantitative match between simulated and EBSD deduced Frobenius norm of the grain (top) surface-averaged partial Nye's tensor. This match was sufficient to admit the simulation predictions as appropriate to quantitatively explain the role of elastic anisotropy and plastic heterogeneity on the generation and extent of the spread of intergranular stresses and plastic strains in the domain. However, if other predictions are expected from the model, then more physics must be added, as has been done in the case of some of the existing thermomechanical models designed for AM applications [5, 7, 8, 9, 14].

7. Conclusion

A small deformation implementation of the thermo-elasto-viscoplastic finite element (TEVP-FE) model with Voce-type isotropic hardening is proposed as the simplest polycrystalline model to study the microstructure evolution of an AM 316L stainless steel subjected to post-process laser scanning. Simulations were performed to study the evolution of stresses and plastic strains over a 2D columnar microstructure generated from a 2D EBSD image of a 3D printed 316L whose surface had been laser scanned using a recently developed coupling between a continuous-wave laser and an SEM (CW Laser-SEM) [4]. The thermal boundary conditions for the simulations were calibrated by fitting the depth and width of the melt pool with those extracted from backscatter electron images. The mechanical response of the simulated melted zone was calibrated to capture the strength increase due to microstructure refinement that occurs due to the applied laser scanning [4]. Simulation-predicted and experimentally measured polar dislocation density (Nye's) tensors were compared.

Following this comparison, the temporal evolution of the stress and plastic strain components was studied on the laser scanned surface and underneath the melt pool. Three critical regions or zones were identified: (a) melted zone (MZ) - region where the melt pool was generated during the laser scan and the thermal strains are negative, (b) heat affected zone (HAZ) - region in the vicinity of the MZ where the temperature was above 400 K and below the solidus (1673 K) during laser scanning and also the region where plastic deformation occurred, and (c) negligible plasticity zone (NPZ) - region beyond the HAZ where the deformation is primarily elastic in nature. Locally plastic deformation values never exceeded 0.05 anywhere in the domain, which justifies the use of a small deformation approximation. The roles of accounting for the strengthening effect of microstructure refinement in the MZ, elastic anisotropy, and plastic heterogeneity on the residual stress and plastic strain distributions were studied in these regions and the following conclusions were drawn:

- Simulations are able to capture the concentration of polar (geometrically necessary) dislocation density along the sides of laser track but poorly predict localization at most locations in the MZ. However, a much better statistical match was obtained upon comparing the Frobenius norm of the grain (top) surface-averaged polar dislocation densities. Approximately 93% of the simulated grains in the MZ had this norm within a factor of 2 of their experimental counterparts; 29% of the grains exhibited a difference of 10% or less. This result sets the benchmark for such comparisons in the future e.g., using more sophisticated models.

- Heterogeneous elastic rotations caused by plastic deformation during laser scanning are the primary contributors to the polar dislocation density (Nye's) tensor; elastic strains have a negligible contribution.

- The domain size and the boundary conditions play a significant role in determining the magnitudes of the stresses and plastic strains as well as the extent to which they propagate into the domain; in comparison, the microstructure plays a less important role on the extent of this propagation. Although the laser scanning occurs in a width of 60 µm (and melting in a width and depth of ~ 35 µm and ~ 6 µm, respectively) at the center of the laser scanned surface, non-negligible residual stresses are generated everywhere in the simulated 400 µm $\times$ 400 µm $\times$ 100 µm domain, with a large portion experiencing only elastic deformation.

- The grain surface-averaged residual normal stress component along the laser scanning direction reaches a value approximately equal to 1.7 GPa for a grain in the MZ. Meanwhile, grain surface-averaged normal plastic strain components reach up to 0.04 in the MZ. These magnitudes are a consequence of the elastic anisotropy, plastic heterogeneity and importantly the strengthening effect due to cellular structure refinement in the MZ.

- Neglecting the strengthening effect due to microstructure refinement results in an error in the stress and plastic strain predictions up to 70% and more than 100%, respectively. The highest errors occur in the MZ for the stresses and in the MZ and HAZ for the plastic strains. Neglecting elastic anisotropy has an important effect only in the NPZ whereas neglecting plastic heterogeneity has a significant effect in the MZ and the HAZ with more than 100% error occurring in plastic strain magnitudes.

Finally, for those researchers interested in testing their model with our results, the EBSD data before and after laser scanning as well as the mesh used to perform the simulations has been provided in supplementary material. Furthermore, suggestions to improve upon our predictions have been provided in section 6.6.

Acknowledgements

NM is grateful to the Ministère de l'Enseignement Supérieur, de la Recherche et de l'Innovation (MESRI), France, for the doctoral scholarship to support his doctoral thesis at the Ecole Polytechnique, Institut Polytechnique de Paris. NM, JGSM and MVU are grateful to the European Research Council (ERC) for their support through the European Union's Horizon 2020 – EXCELLENT SCIENCE – research and innovation program (grant agreement number 946959). The authors thank LMS for providing financial support to build the CW Laser-SEM system.

References

[1] A. S. Wu, D. W. Brown, M. Kumar, G. F. Gallegos, W. E. King, An experimental investigation into additive manufacturing-induced residual stresses in 316L stainless steel, Metallurgical and Materials Transactions A 45 (13) (2014) 6260–6270. doi:10.1007/s11661-014-2549-x.

[2] A. J. Dunbar, E. R. Denlinger, J. Heigel, P. Michaleris, P. Guerrier, R. Martukanitz, T. W. Simpson, Development of experimental method for in situ distortion and temperature measurements during the laser powder bed fusion additive manufacturing process, Additive Manufacturing 12 (2016) 25–30. doi:10.1016/j.addma.2016.04.007.

[3] Z. Xiao, C. Chen, H. Zhu, Z. Hu, B. Nagarajan, L. Guo, X. Zeng, Study of residual stress in selective laser melting of Ti6Al4V, Materials & Design 193 (2020) 108846. doi:10.1016/j.matdes.2020.108846.

[4] J. G. Santos Macías, K. Chen, A. Tanguy, M. Vallet, L. Cornet, V. Michel, M. V. Upadhyay, Micron-sized lasering improves mechanical behaviour of 3D printed steels, (under review).

[5] M. Lindroos, T. Pinomaa, A. Antikainen, J. Lagerbom, J. Reijonen, T. Lindroos, T. Andersson, A. Laukkanen, Micromechanical modeling approach to single track deformation, phase transformation and residual stress evolution during selective laser melting using crystal plasticity, Additive Manufacturing 38 (2021) 101819. doi:https://doi.org/10.1016/j.addma.2020.101819.

[6] D. Rosenthal, The theory of moving sources of heat and its application to metal treatments, Journal of Fluids Engineering 68 (8) (1946) 849–865. doi:10.1115/1.4018624.

[7] N. Grilli, D. Hu, D. Yushu, F. Chen, W. Yan, Crystal plasticity model of residual stress in additive manufacturing using the element elimination and reactivation method, Computational Mechanics 69 (2022) 825–845. doi:10.1007/s00466-021-02116-z.

[8] D. Hu, N. Grilli, L. Wang, M. Yang, W. Yan, Microscale residual stresses in additively manufactured stainless steel: Computational simulation, Journal of the Mechanics and Physics of Solids 161 (2022) 104822. doi:https://doi.org/10.1016/j.jmps.2022.104822.

[9] D. Hu, N. Grilli, W. Yan, Dislocation structures formation induced by thermal stress in additive manufacturing: Multiscale crystal plasticity modeling of dislocation transport, Journal of the Mechanics and Physics of Solids 173 (2023) 105235. doi:https://doi.org/10.1016/j.jmps.2023.105235.

[10] L. Kuna, A. J. Birnbaum, K. Teferra, A framework for predicting residual mechanical response fields for laser powder bed fusion at the polycrystalline length scale 78 103830. doi:10.1016/j.addma.2023.103830.
URL https://www.sciencedirect.com/science/article/pii/S2214860423004438

[11] A. Tanguy, M. V. Upadhyay, J. G. Santos Macías, Système pour traiter par laser à onde continue et caractériser par MEB un échantillon, (Patent Pending - deposited on 16 December 2022) (2022).

[12] B. Beausir, J. Fundenberger, Analysis tools for electron and x-ray diffraction, ATEX-software, www.atex-software.eu, Université de Lorraine-Metz 201 (7) (2017).

[13] W. Pantleon, Resolving the geometrically necessary dislocation content by conventional electron backscattering diffraction, Scripta Materialia 58 (11) (2008) 994–997. doi:10.1016/j.scriptamat.2008.01.050.

[14] M. Lindroos, T. Pinomaa, K. Ammar, A. Laukkanen, N. Provatas, S. Forest, Dislocation density in cellular rapid solidification using phase field modeling and crystal plasticity, International Journal of Plasticity 148 (2022) 103139. doi:https://doi.org/10.1016/j.ijplas.2021.103139.
URL https://www.sciencedirect.com/science/article/pii/S0749641921002072

[15] J. Nye, Some geometrical relations in dislocated crystals, Acta Metallurgica 1 (2) (1953) 153–162. doi:https://doi.org/10.1016/0001-6160(53)90054-6.

[16] M. V. Upadhyay, On the thermo-mechanical theory of field dislocations in transient heterogeneous temperature fields, Journal of the Mechanics and Physics of Solids 145 (2020) 104150. doi:10.1016/j.jmps.2020.104150.

[17] R. J. Asaro, A. Needleman, Overview no. 42 Texture development and strain hardening in rate dependent polycrystals, Acta Metallurgica 33 (6) (1985) 923–953. doi:https://doi.org/10.1016/0001-6160(85)90188-9.

[18] H. J. Frost, M. F. Ashby, Deformation-mechanism Maps: The plasticity and creep of metals and ceramics, Franklin Book Company, Incorporated, 1982.

[19] C. Tome, G. R. Canova, U. F. Kocks, N. Christodoulou, J. J. Jonas, The relation between macroscopic and microscopic strain hardening in F.C.C. polycrystals, Acta Metallurgica 32 (10) (1984) 1637–1653. doi:https://doi.org/10.1016/0001-6160(84)90222-0.

[20] E. Voce, The relationship between stress and strain for homogeneous deformation, Journal of the Institute of Metals 74 (1948) 537–562.

[21] S. Tiem, M. Berveiller, G. Canova, Grain shape effects on the slip system activity and on the lattice rotations, Acta Metallurgica 34 (11) (1986) 2139–2149. doi:https://doi.org/10.1016/0001-6160(86)90159-8.

[22] E. M. B. Campello, A description of rotations for DEM models of particle systems, Computational Particle Mechanics 2 (2) (2015) 109–125. doi:10.1007/s40571-015-0041-z.

[23] M. Alnæs, J. Blechta, J. Hake, A. Johansson, B. Kehlet, A. Logg, C. Richardson, J. Ring, M. E. Rognes, G. N. Wells, The FEniCS project version 1.5, Archive of Numerical Software 3 (100) (2015). doi:10.11588/ans.2015.100.20553.

[24] T. Helfer, B. Michel, J.-M. Proix, M. Salvo, J. Sercombe, M. Casella, Introducing the open-source mfront code generator: Application to mechanical behaviours and material knowledge management within the PLEIADES fuel element modelling platform, Computers & Mathematics with Applications 70 (5) (2015) 994–1023. doi:https://doi.org/10.1016/j.camwa.2015.06.027.

[25] T. Helfer, J. Bleyer, T. Frondelius, I. Yashchuk, T. Nagel, D. Naumov, The MFrontGenericInterfaceSupport project, Journal of Open Source Software 5 (48) (2003). doi:10.21105/joss.02003.

[26] C. S. Kim, Thermophysical properties of stainless steels, Office of Scientific and Technical Information, 1975. doi:10.2172/4152287.

[27] E. D. Cyr, M. Mohammadi, R. K. Mishra, K. Inal, A three dimensional (3D) thermo-elasto-viscoplastic constitutive model for FCC polycrystals, International Journal of Plasticity 70 (2015) 166–190. doi:10.1016/j.ijplas.2015.04.001.

[28] U. F. Kocks, Laws for work-hardening and low-temperature creep, Journal of Engineering Materials and Technology 98 (1) (1976) 76–85. doi:10.1115/1.3443340.

[29] E. Puchi Cabrera, High temperature deformation of 316l stainless steel 17 (2) 155–161, publisher: Taylor & Francis _eprint: https://doi.org/10.1179/026708301101509944. doi:10.1179/026708301101509944.
URL https://doi.org/10.1179/026708301101509944

[30] F. Khodabakhshi, M. H. Farshidianfar, A. P. Gerlich, M. Nosko, V. Trembošová, A. Khajepour, Microstructure, strain-rate sensitivity, work hardening, and fracture behavior of laser additive manufactured austenitic and martensitic stainless steel structures 756 545–561. doi:10.1016/j.msea.2019.04.065.
URL https://www.sciencedirect.com/science/article/pii/S0921509319305295

[31] M. Güden, S. Enser, M. Bayhan, A. Taşdemirci, H. Yavaş, The strain rate sensitive flow stresses and constitutive equations of a selective-laser-melt and an annealed-rolled 316l stainless steel: A comparative study 838 142743. doi:10.1016/j.msea.2022.142743.
URL https://www.sciencedirect.com/science/article/pii/S0921509322001514

[32] M. Messner, V. Phan, T. Sham, Development of the technical basis of a unified viscoplastic model of 316h stainless steel for incorporation into ASME division 5. doi:10.2172/1602400.
URL https://www.osti.gov/servlets/purl/1602400/

[33] M. Upadhyay, L. Capolungo, V. Taupin, C. Fressengeas, R. Lebensohn, A higher order elasto-viscoplastic model using fast Fourier transforms: Effects of lattice curvatures on mechanical response of nanocrystalline metals, International Journal of Plasticity 83 (2016) 126–152. doi:https://doi.org/10.1016/j.ijplas.2016.04.007.

[34] M. Biegler, B. Graf, M. Rethmeier, In-situ distortions in LMD additive manufacturing walls can be measured with digital image correlation and predicted using numerical simulations, Additive Manufacturing 20 (2018) 101–110. doi:https://doi.org/10.1016/j.addma.2017.12.007.

[35] C. Sandstrom, Voxel2tet, Tech. rep., Chalmers University of Technology, original-date: 2016-08-17 (2016).
URL https://github.com/CarlSandstrom/Voxel2Tet

[36] C. Dobrzynski, MMG3D: User Guide, Technical Report RT-0422, INRIA (Mar. 2012).
URL https://inria.hal.science/hal-00681813

[37] P. Mercelis, J.-P. Kruth, Residual stresses in selective laser sintering and selective laser melting, Rapid Prototyping Journal 12 (2006) 254–265. doi:10.1108/13552540610707013.

[38] R. Sivakumar, B. L. Mordike, Laser melting of plasma sprayed ceramic coatings, Surface Engineering 4 (2) (1988) 127–140. doi:10.1179/sur.1988.4.2.127.

[39] J. Grum, R. Šturm, Residual stresses on flat specimens of different kinds of grey and nodular irons after laser surface remelting, Materials Science and Technology 17 (4) (2001) 419–424. doi:10.1179/026708301101510159.

[40] C. Chabrol, A. B. Vannes, Residual stresses induced by laser surface treatment, Springer Netherlands, Dordrecht, 1986, Ch. 5c, pp. 435–450. doi:10.1007/978-94-009-4468-8-38.

[41] J. Grum, R. Šturm, A new experimental technique for measuring strain and residual stresses during a laser remelting process, Journal of Materials Processing Technology 147 (3) (2004) 351–358. doi:10.1016/j.jmatprotec.2004.01.007.

[42] R. Quey, M. Kasemer, The neper/FEPX project: Free / open-source polycrystal generation, deformation simulation, and post-processing 1249 (1) 012021, publisher: IOP Publishing. doi:10.1088/1757-899X/1249/1/012021.
URL https://dx.doi.org/10.1088/1757-899X/1249/1/012021

[43] M. A. Groeber, M. A. Jackson, DREAM.3d: A digital representation environment for the analysis of microstructure in 3d 3 (1) 56–72. doi:10.1186/2193-9772-3-5.
URL https://doi.org/10.1186/2193-9772-3-5

[44] P. Seibert, A. Raßloff, K. Kalina, M. Ambati, M. Kästner, Microstructure characterization and reconstruction in python: MCRpy. arXiv:

2207.04652[cond-mat], doi:10.48550/arXiv.2207.04652.
URL http://arxiv.org/abs/2207.04652

[45] A. F. Chadwick, P. W. Voorhees, The development of grain structure during additive manufacturing 211 116862. doi:10.1016/j.actamat.2021.116862.
URL https://linkinghub.elsevier.com/retrieve/pii/S1359645421002421

[46] O. Zinovieva, A. Zinoviev, V. Ploshikhin, Three-dimensional modeling of the microstructure evolution during metal additive manufacturing 141 207–220. doi:10.1016/j.commatsci.2017.09.018.
URL https://www.sciencedirect.com/science/article/pii/S0927025617304986

[47] Y. Yu, Y. Li, F. Lin, W. Yan, A multi-grid cellular automaton model for simulating dendrite growth and its application in additive manufacturing 47 102284. doi:10.1016/j.addma.2021.102284.
URL https://www.sciencedirect.com/science/article/pii/S2214860421004449

[48] T. M. Rodgers, J. D. Madison, V. Tikare, Simulation of metal additive manufacturing microstructures using kinetic monte carlo 135 78–89. doi:10.1016/j.commatsci.2017.03.053.
URL https://www.sciencedirect.com/science/article/pii/S0927025617301751

[49] S. Sunny, H. Yu, R. Mathews, A. Malik, W. Li, Improved grain structure prediction in metal additive manufacturing using a dynamic kinetic monte carlo framework 37 101649. doi:10.1016/j.addma.2020.101649.
URL https://www.sciencedirect.com/science/article/pii/S2214860420310216

[50] M. P. Echlin, M. Straw, S. Randolph, J. Filevich, T. M. Pollock, The TriBeam system: Femtosecond laser ablation in situ SEM 100 1–12. doi:10.1016/j.matchar.2014.10.023.
URL https://www.sciencedirect.com/science/article/pii/S104458031400326X

[51] G. D. Lima-Chaves, M. V. Upadhyay, Finite element implementation of the thermal field dislocation mechanics model: Study

of temperature evolution due to dislocation activity, Computer Methods in Applied Mechanics and Engineering 421 (2024) 116763. doi:https://doi.org/10.1016/j.cma.2024.116763.
URL https://www.sciencedirect.com/science/article/pii/S0045782524000197

[52] J. Ahrens, B. Geveci, C. Law, 36 - ParaView: An end-user tool for large-data visualization, in: C. D. Hansen, C. R. Johnson (Eds.), Visualization Handbook, Butterworth-Heinemann, pp. 717–731. doi:10.1016/B978-012387582-2/50038-1.
URL https://www.sciencedirect.com/science/article/pii/B9780123875822500381

Appendix

A.1. TEVP-FE Algorithm

Algorithm A.1 TEVP-FE

Input: Mesh (Ω), timestep (dt_{init}), $\boldsymbol{u}(\cdot,0), \theta(\cdot,0), \theta^t(\cdot,0)$, Material parameters ($\mathbb{C}, \mathbb{M}, \boldsymbol{\gamma^\theta}, \boldsymbol{K}, \rho, c_v, n, \tau_0, \tau_1, \Theta_0, \Theta_1$), Initial orientations ($\boldsymbol{g}^t_{ori}$)
Result: u, θ, $\boldsymbol{\sigma}, \boldsymbol{\varepsilon}$, $\boldsymbol{\varepsilon}^e, \boldsymbol{\varepsilon}^p, \boldsymbol{g}_{ori}$, $\boldsymbol{\alpha}_{\omega^e}$

Begin
$dt \leftarrow dt_{init}$
while $t < t_{max}$ **do**
  try
    Solve equation (19) for θ using a linear solver
    Solve equation (20) for $\boldsymbol{u}$ using a Newton-Raphson solver:
      Solve for $\left(\frac{d\boldsymbol{\sigma}}{d\Delta\boldsymbol{\varepsilon}}\right)$ using a second (embedded) Newton-Raphson shown in appendix A.2
      Compute $R_u = \int_{\partial\Omega} \boldsymbol{t} \cdot \hat{\boldsymbol{u}} ds - \int_\Omega \boldsymbol{\sigma} : \nabla \hat{\boldsymbol{u}} dx$
      Compute Jacobian $\boldsymbol{J_u} = \frac{\partial R_u}{\partial \boldsymbol{u}} = \frac{\partial R_u}{\partial \boldsymbol{\sigma}} : \frac{\partial \boldsymbol{\sigma}}{\partial \Delta\boldsymbol{\varepsilon}} : \frac{\partial \Delta\boldsymbol{\varepsilon}}{\partial \boldsymbol{u}}$
      Solve $\Delta\boldsymbol{u} = -\boldsymbol{J_u}^{-1} R_u$
      Update $\boldsymbol{u} \leftarrow \boldsymbol{u}^t + \Delta\boldsymbol{u}$
    Update orientation
    Output solution
    Update $(\boldsymbol{u}^t, \theta^t) \leftarrow (\boldsymbol{u}, \theta)$
    Update time: $t \leftarrow t + dt$
  except convergence error
    Bisect: $dt \leftarrow dt/2$
    if $dt \leq dt_{init}/16$ **then**
      Raise: runtime error
  continue
end while

A.2. Computing the consistent tangent operator

Let $\boldsymbol{Y}$ be a vector containing the set of internal variables: elastic strain tensor components ε^e_{ij} and the shear slip γ^s on all slip systems s:

$$\boldsymbol{Y} = \begin{bmatrix} \boldsymbol{\varepsilon}^e \\ \gamma^s \end{bmatrix} \rightarrow \Delta\boldsymbol{Y} = \begin{bmatrix} \Delta\boldsymbol{\varepsilon}^e \\ \Delta\gamma^s \end{bmatrix} \tag{A.1}$$

where Δ represents the increment of an internal variable during the time increment Δt. The consistent tangent operator is obtained as:

$$\frac{d\boldsymbol{\sigma}}{d\Delta\boldsymbol{\varepsilon}} = \frac{\partial\boldsymbol{\sigma}}{\partial\Delta\boldsymbol{\varepsilon}} + \left[\frac{\partial\boldsymbol{\sigma}}{\partial\Delta\boldsymbol{Y}}\right]\left[\frac{\partial\Delta\boldsymbol{Y}}{\partial\Delta\boldsymbol{\varepsilon}}\right] \tag{A.2}$$

$\boldsymbol{F}$ is constructed as a vector of implicit equations from the constitutive equations (9) and (12) as:

$$\boldsymbol{F}(\Delta\boldsymbol{\varepsilon}^e, \Delta\gamma^s) = \begin{bmatrix} \boldsymbol{f}_{\Delta\boldsymbol{\varepsilon}^e} \\ \boldsymbol{f}_{\Delta\gamma^s} \end{bmatrix} = \begin{bmatrix} \Delta\boldsymbol{\varepsilon}^e + \sum_s^{Nss} \Delta\gamma^s \ \boldsymbol{m}^s - \Delta\boldsymbol{\varepsilon} \\ \Delta\gamma^s - \Delta t \ \dot{\gamma}_0^s \left(\frac{|\tau^s|}{\tau_c^s}\right) sign(\tau^s) \end{bmatrix} = 0 \tag{A.3}$$

where

$$\tau_c^s = \tau_0^s + (\tau_1^s + \Theta_1^s\Gamma)\left(1 - exp\left(-\left|\frac{\Theta_0^s}{\tau_1^s}\right|\Gamma\right)\right)$$

Differentiating equation (A.3) with respect to $\Delta\boldsymbol{\varepsilon}$:

$$\frac{d\boldsymbol{F}}{d\Delta\boldsymbol{\varepsilon}} = \left[\frac{\partial\boldsymbol{F}}{\partial\Delta\boldsymbol{\varepsilon}}\right] + \left[\frac{\partial\boldsymbol{F}}{\partial\Delta\boldsymbol{Y}}\right]\left[\frac{\partial\Delta\boldsymbol{Y}}{\partial\Delta\boldsymbol{\varepsilon}}\right] = 0 \tag{A.4}$$

$$\left[\frac{\partial\Delta\boldsymbol{Y}}{\partial\Delta\boldsymbol{\varepsilon}}\right] = -\left[\boldsymbol{J}\right]^{-1}\left[\frac{\partial\boldsymbol{F}}{\partial\Delta\boldsymbol{\varepsilon}}\right] \tag{A.5}$$

where $[J] = [\partial\boldsymbol{F}/\partial\Delta\boldsymbol{Y}]$ is the Jacobian of the implicit system of equations derived from the constitutive laws. The resulting derivative from equation (A.5) is inserted into equation (A.2) to compute $(d\boldsymbol{\sigma}/d\Delta\boldsymbol{\varepsilon})$.

A.3. Fitting $\boldsymbol{\mu(\theta)}$

Below are the fitted equations of the multiplication factor $\mu(\theta)$ following the proportional degradation trend of stress-strain curves [34] for the temperature dependency of Voce hardening parameters.

$$\mu_{\tau_0}(\theta) = \begin{cases} 12.70353 & -2.26726\times10^{-2}\times\theta \\ & +1.35721\times10^{-5}\times\theta^2 \\ & -2.71744\times10^{-9}\times\theta^3 \quad 1173K < \theta \leq 1673K \\ 1.98224 & -4.62050\times10^{-3}\times\theta \\ & +5.07243\times10^{-6}\times\theta^2 \\ & -1.94842\times10^{-9}\times\theta^3 \quad 300K \leq \theta \leq 1173K \end{cases} \tag{A1}$$

$$\mu_{\tau_1}(\theta) = \begin{cases} 4.75941 \times 10^{-2} + \left(\dfrac{0.95240}{1 + \left(\dfrac{\theta}{1040.523} \right)^{10.064}} \right) \\ \qquad\qquad\qquad\qquad\qquad\qquad 300K \leq \theta \leq 1673K \end{cases} \tag{A2}$$

$$\mu_{\Theta_0}(\theta) = \begin{cases} -7.02581 \quad \times 10^{-6} + \left(\dfrac{0.69143}{\left(1 + \left(\dfrac{\theta}{1212.722} \right)^{35.73236} \right)} \right) \\ \qquad\qquad\qquad\qquad\qquad\qquad 1173K < \theta \leq 1673K \\ 2.26922 \quad -6.40022 \times 10^{-3} \times \theta \\ \qquad\quad +8.27602 \times 10^{-6} \times \theta^2 \\ \qquad\quad -3.48138 \times 10^{-9} \times \theta^3 \quad 300K \leq \theta \leq 1173K \end{cases} \tag{A3}$$

$$\mu_{\Theta_1}(\theta) = \begin{cases} 7.92198 \quad -1.53633 \times 10^{-4} \times \theta \\ \qquad\quad +9.95078 \times 10^{-6} \times \theta^2 \\ \qquad\quad -2.15064 \times 10^{-9} \times \theta^3 \quad 1173K < \theta \leq 1673K \\ -13.32002 \quad +2.93492 \times 10^{-2} \times \theta \\ \qquad\quad -1.52517 \times 10^{-5} \times \theta^2 \quad 973K < \theta \leq 1173K \\ 1.13517 \quad -6.82732 \times 10^{-4} \times \theta \\ \qquad\quad +9.65111 \times 10^{-7} \times \theta^2 \\ \qquad\quad -6.37325 \times 10^{-10} \times \theta^3 \quad 300K \leq \theta \leq \ 973K \end{cases} \tag{A4}$$

A.4. Output representation procedure

Output and visualization of the simulated and experimental data require some precision. The open source Paraview [52] has been used to perform post-process computations and to generate contour plots.

The stresses and all deformation measures are computed at the integration points of the mesh elements, while the temperature and displacement vector are computed at the nodal points. In most cases, for visualization, integration point variables are projected using a first order continuous Galerkin approximation (CG1 in FEniCS) to the nodes.

The model and experiment comparison is performed using the polar dislocation density in the residual state. The following procedure is used to perform a one to one comparison. The simulated partial polar density from equation (6) is computed as $\boldsymbol{\alpha}_{\omega^e} = \nabla \times \boldsymbol{\omega}^e = -\nabla \times \text{skew}(\nabla \boldsymbol{u} - \boldsymbol{U}^p)$, where $\boldsymbol{\omega}^e = \text{skew}(\nabla \boldsymbol{u} - \boldsymbol{U}^p)$ is first computed by projecting the corresponding variables to a first order interpolated discontinuous Galerkin (DG1 in FEniCS) space. Then, $\nabla \times \boldsymbol{\omega}^e$ is computed in this DG1 space and finally projected using a CG1 operation onto the nodes for visualization. This series of operations was the only one possible with the available software.

The 2D EBSD data with the computed polar dislocation densities $\boldsymbol{\alpha}_{\text{exp}}$ are acquired from ATEX [12] as pixelated data, which is transferred without interpolation to a structured VTK grid for visualization in Paraview.

The 1-norm of the experimental and simulated partial dislocation density tensors shown in Figure 4 are computed on their respective grids.

The Frobenius norm has been used for the quantitative comparison shown in Figure 5. For a second order tensor $\boldsymbol{A}$, its Frobenius norm is defined as

$$\|\boldsymbol{A}\|_F := \sqrt{\sum_{i=1}^{3}\sum_{i=1}^{3} A_{ij}^2} \tag{A5}$$

The geometric interpretation of this norm is that it is the longest distance in a parallelopiped, whose sides are formed by the singular values of a matrix (eigenvalues for symmetric matrices); in the case of a second order tensor in 3D, this norm corresponds to the longest diagonal of the cuboid formed by the eigenvalues of the tensor. By definition, this norm is rotational invariant.

For the partial polar dislocation density tensors, the sum is performed with only those components whose values are available. For the quantitative comparison of the simulated $\|\boldsymbol{\alpha}_{\omega^e}\|_F$ with $\|\boldsymbol{\alpha}_{\text{exp}}\|_F$, these norms are first computed on their respective grids in Paraview i.e., $\|\boldsymbol{\alpha}_{\omega^e}\|_F$ is computed at the nodal points of the FE mesh and $\|\boldsymbol{\alpha}_{\text{exp}}\|_F$ is computed at the pixelized

2D EBSD grid. Then, both quantities are resampled (using the function Resample to Image in Paraview) onto a common structured pixelated grid and the ratio shown in Figure 5 was computed. A grid spacing convergence study was undertaken and $\sim 0.25\,\mu m$ was identified as the minimum size that provides an unaltered solution.

Supplementary figures

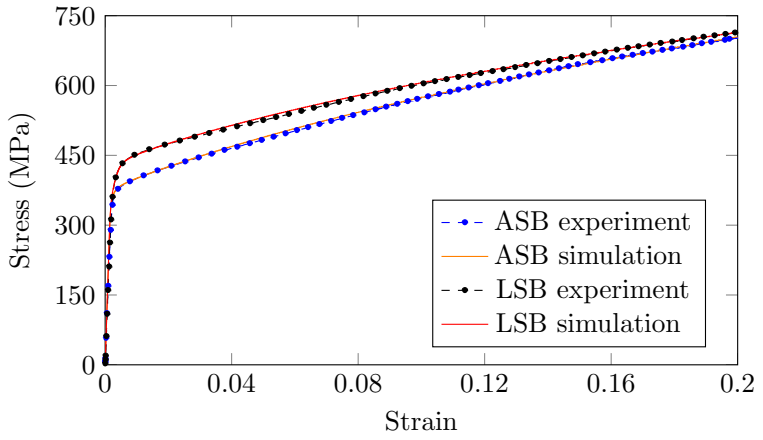

Figure S1: Voce parameter fitted stress-strain plots at 300 K using the uniaxial tensile test data of as-built (ASB) and lasered (LSB) samples obtained from [4].

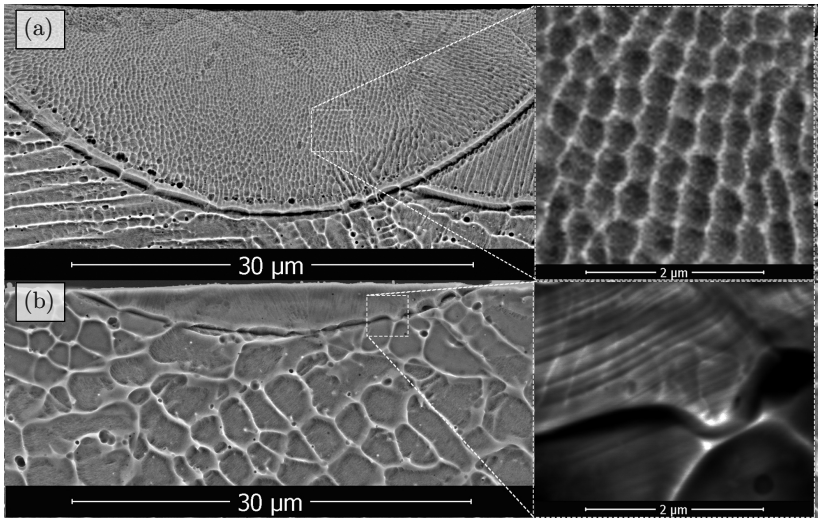

Figure S2: Comparison of Cr-Mo cellular microstructure generated during (a) multi-pass laser scanning at 35W power, 50 mm/s scan speed and 60 µm spot size, and (b) single pass laser scanning at 24W power, 500 mm/s scan speed and 60 µm spot size. Zoomed-in views of the microsegregation cells show that the cell size in both cases is of similar order. The images have been adapted from [4].

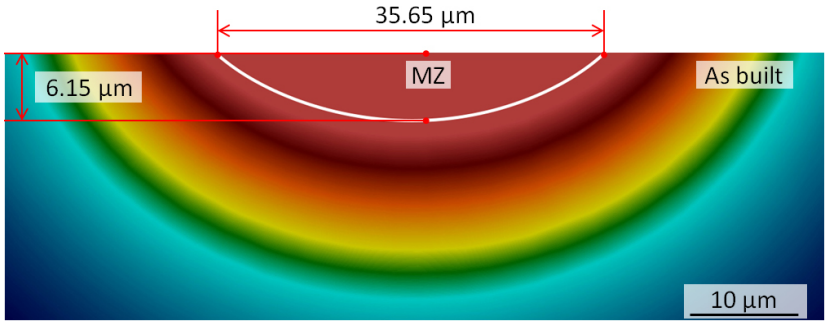

Figure S3: Cross-sectional view of the temperature field depicting the simulated melt pool.

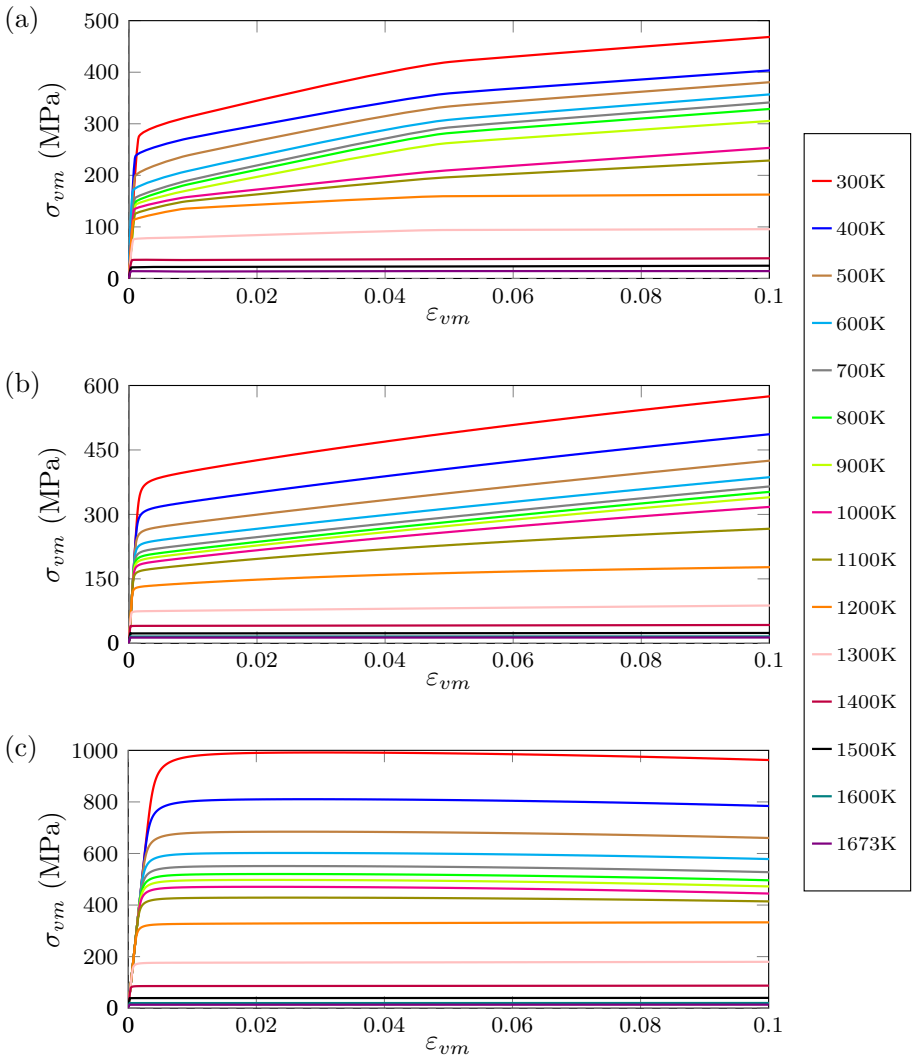

Figure S4: Isothermal stress-strain behavior at different temperatures of (a) ANSI 316L SS adapted from [34], fitted (b) As-built zone AM 316L SS and (b) MZ refined AM 316L SS materials based on the temperature-dependent hardening parameters specified in Table 1, the temperature dependency of (b) and (c) were adapted from (a)[34].

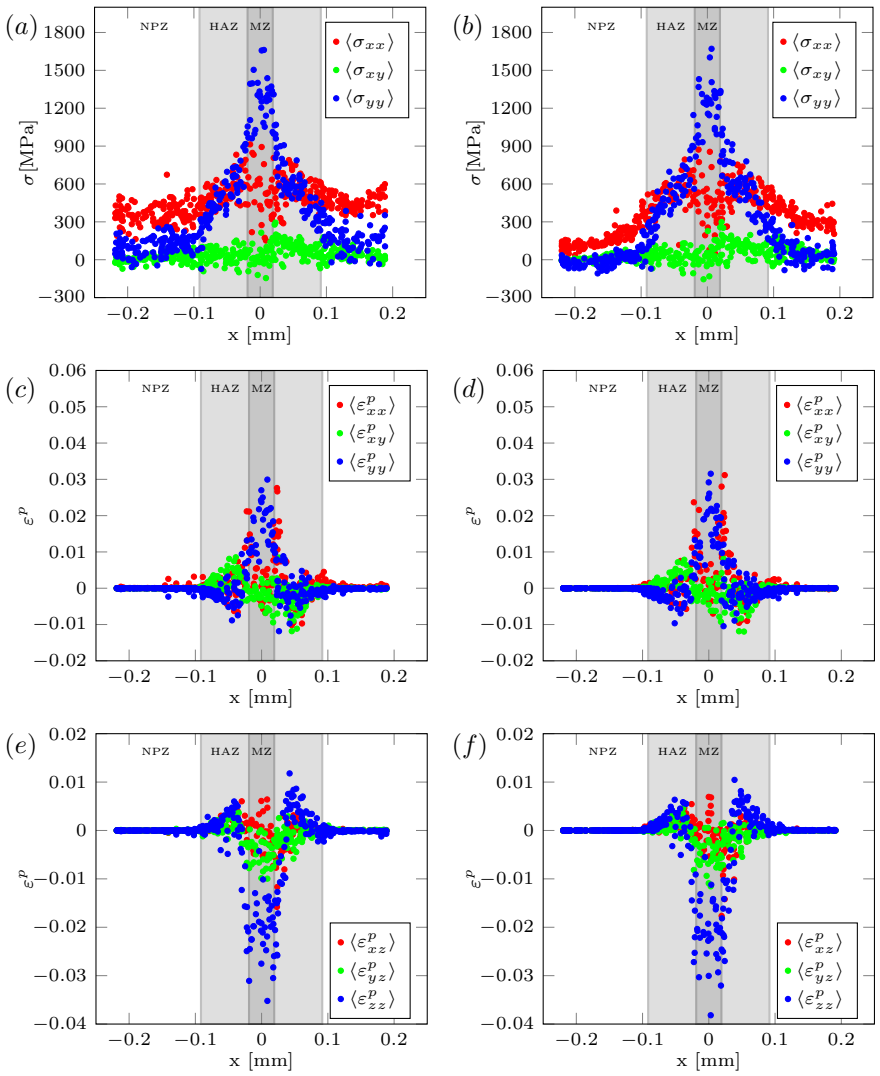

Figure S5: Residual stress and plastic strain components averaged on the top surface over each grain plotted as a function of the distance along x from the center of the laser scan path for the 50 µm and 100 µm depth microstructures. The residual state MZ, HAZ and NPZ are demarcated using grey shaded or unshaded regions.